Finite Elements in Analysis and Design 152 (2018) 27–45

Contents lists available at ScienceDirect

Finite Elements in Analysis and Design

journal homepage: www.elsevier.com/locate/finel

A linear complete extended finite element method for dynamic fracture simulation with non-nodal enrichments

Iman Asareh [a], Tae-Yeon Kim [b,*], Jeong-Hoon Song [c,**]

[a] Department of Civil and Environmental Engineering, University of South Carolina, Columbia, SC 29208, USA
[b] Civil Infrastructure and Environmental Engineering, Khalifa University of Science and Technology, Abu Dhabi 127788, United Arab Emirates
[c] Department of Civil, Environmental and Architectural Engineering, University of Colorado, Boulder, CO 80309, USA

ARTICLE INFO

2010 MSC:
00-01
99-00

Keywords:
Non-nodal enrichment
Dynamic fracture
Linear complete
Cohesive law

ABSTRACT

A linear complete extended finite element method for arbitrary dynamic crack is presented. In this method, strong and weak discontinuities are assigned to a set of non-nodal points on the interface, whereby the discontinuous functions across the interface are reproduced by extended interpolation. The enrichments are described to reproduce both the constants and linear functions on sides of the interface, which are critical for finite element convergence. A key feature of this method is that the enrichment descriptions and the finite element mesh are optimally uncoupled; the element nodes are not enriched facilitating the treatment of crack modeling in object-oriented programs. The enrichment variables are *physically-based* quantities which lead to a strong imposition of both the Dirichlet boundary conditions and the interface conditions. The convergence of the method is validated through static simulations from linear elastic fracture mechanics. The efficacy of the method for modeling dynamic crack propagation is demonstrated through two benchmark problems.

1. Introduction

The extended finite element method (XFEM) [1,2] exploits a local partition of unity [3] to enhance the approximation space by non-polynomial bases. One advantage of the XFEM over the finite element method (FEM) is that it can model the discontinuities in the solution to a given PDE in a local domain without remeshing. However, in a standard XFEM, finite element mesh is locally incorporated in the description of enrichments, i.e., the finite element nodes which belong to mesh, but not to the interface, are enriched to describe a discontinuity across an interface. This will arise many difficulties in XFEM reproducing capabilities, or even the programming implementation [4].

Some remedies have been provided in early XFEM studies to address the difficulties arisen due to dependency between the mesh and the enrichments. Examples include shifting the approximation to hold the Kronecker-δ property introduced by Belytschko et al. [5], treating blending elements to correct reproducing conditions addressed by Chessa et al. [6] and Fries [7], and enriching a subset of element nodes to satisfy C^0-continuity conditions between the enriched element and its contiguous elements discussed by Belytschko et al. [8] and Zi et al. [9]. Moreover, Song et al. [10] introduced the phantom node method to model the discontinuities independently of the mesh. This approach was further investigated for shell elements in Refs. [11,12]. As alternative classes of methods, the cracking-particle method [13] and dual-horizon peridynamics [14,15] in meshfree methods have been successfully used in crack modeling. In these approaches, the crack is modeled by splitting particles on sides of the interface whereby the strong discontinuity is captured independent of the mesh.

One of the main difficulties in enriching finite element nodes is the imposition of Dirichlet boundary conditions. Since the interpretation of enrichment variables is difficult, the non-smooth boundary constraints [16] and interface constraints [17,18] are weakly enforced, i.e., they are imposed in the weak form using Lagrange multiplier techniques. Moreover, some treatments introduced for the XFEM cannot be applied together. For instance, as lumped mass matrices are crucial for the efficiency of the explicit time stepping, Menouillard et al. [19] introduced a mass lumping strategy which is applicable to unshifted enrichment functions. To circumvent such difficulties, it is desirable to have a technique that can describe discontinuities across the interfaces independent of finite element mesh.

Another main difficulty in the standard XFEM is the programming implementation. Since the finite element nodes in a local element are

* Corresponding author.
** Corresponding author.
E-mail addresses: taeyeon.kim@ku.ac.ae (T.-Y. Kim), jh.song@colorado.edu (J.-H. Song).

https://doi.org/10.1016/j.finel.2018.09.002
Received 12 August 2018; Received in revised form 16 September 2018; Accepted 18 September 2018
Available online 5 October 2018

used to construct the enrichments, the element object and the enrichment object in an object-oriented program (OOP) become dependent. This feature clearly violates the OOP principle of abstraction as the discontinuities in a continuum are independent from the mesh. As a consequence, several difficulties arise in both XFEM implementation and post-processing steps [20,21].

To overcome these difficulties, a non-nodal enrichment technique [22] was introduced to describe the discontinuities across an interface with minimal incorporating of finite element mesh into enrichment descriptions. In this approach, a partition of unity is not constructed, so the element nodes are not enriched. Instead, discontinuities are defined for a set of non-nodal points on the interface to reproduce discontinuous fields across the interface. The enrichments in Ref. [22] reproduce strong discontinuities in displacement fields, which can well reflect the nature of a crack. Furthermore, since the enrichment parameters were selected to be the displacement jumps which are, in fact, *physically-based* variables related to the crack, the interface boundary conditions can be easily treated in the strong form as Dirichlet boundary conditions.

The main objective of this study is to enhance the interpolation in Ref. [22] to reproduce not only the strong discontinuities in displacement fields but also the discontinuities in their first derivatives. To this end, a new set of enrichment bases is introduced to non-nodal points on the interface to reproduce the jumps in the first derivatives. This leads to a completely local enrichment without shifting techniques and a linear complete approximation, i.e., the interpolation can reproduce both rigid body motion and constant strain state on both sides of the interface.

The remainder of the paper is as follows. In section 2, we provide the non-nodal enrichment displacement for a linear complete approximation in one- and two-dimensional problems. Section 3 presents the strong form, the weak form and the discretizations for dynamic analysis. It also introduce a quadrature rule developed for non-nodal enrichment methods. Finally, section 4 provides several numerical studies analyzed by the method for static and dynamic simulations.

2. Enriched displacement fields for discontinuity

We consider a two-dimensional body Ω with its boundary Γ in the initial configuration, as shown in Fig. 1. The body includes a crack with a surface discontinuity denoted by Γ_c. Two sides of this discontinuity are signed by a continuous level set function $f(\mathbf{X})$ so that $f(\mathbf{X})=0$ gives the discontinuity surface. The level set function f can be described by the signed distance function as

$$f(\mathbf{X}) = \min_{\overline{\mathbf{X}}\in\Gamma_c} \|\mathbf{X}-\overline{\mathbf{X}}\| \ \text{sign}(\mathbf{n}^+\cdot(\overline{\mathbf{X}}-\mathbf{X})) \tag{1}$$

where $\overline{\mathbf{X}}$ is the closest point on the interface to $\mathbf{X}$ and $\|\cdot\|$ denotes the Euclidean norm. The unit normal vector $\mathbf{n}^+$ is perpendicular to the discontinuity surface where the level set is positive, i.e., $f>0$.

We extend the interpolation so that it can capture two discontinuities: a strong discontinuity across the crack surface which can be represented with a jump in displacements and a weak discontinuity which can be considered as a jump in strains. It can be shown that when the interpolation reproduces independent linear functions on sides of the interface, then such discontinuities can be captured. Therefore, the interpolation is enriched to reproduce two discontinuous displacement fields: a displacement field with a strong discontinuity denoted by Φ^{u} which is defined using the Heaviside function, i.e.,

$$\Phi^{\mathrm{u}} = H(f(\mathbf{X})) = \begin{cases} 0 & \text{if } f<0, \\ 1 & \text{if } f>0, \end{cases} \tag{2}$$

and another displacement field with a weak discontinuity, i.e., a discontinuity in its first derivative denoted by $\Phi^{\nabla \mathrm{u}}$ which is defined as

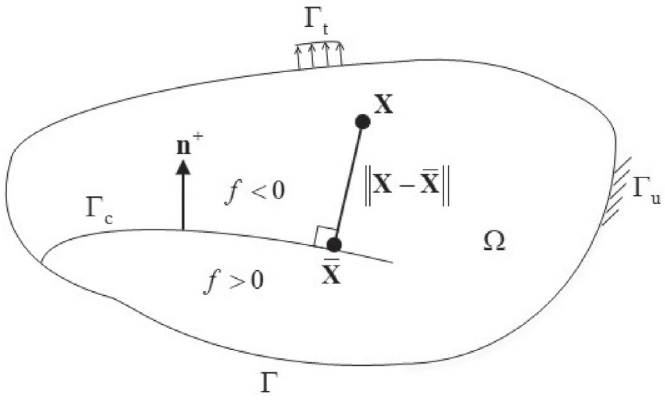

Fig. 1. A two-dimensional body with a crack in material coordinates.

$$\Phi^{\nabla \mathrm{u}} = H(f(\mathbf{X}))\times f(\mathbf{X}) = \begin{cases} 0 & \text{if } f<0, \\ f(\mathbf{X}) & \text{if } f>0. \end{cases} \tag{3}$$

For each discontinuity, a physically – based variable which can best reflect the nature of the discontinuity is defined as an enrichment parameter and assigned to non-nodal points on the surface of discontinuity. In the following, we first construct the enrichments for a linear element in one dimension and then for a linear triangular element in two dimensions.

2.1. Representation of a crack with non-nodal enrichment parameters for 2-node linear elements

We consider a one-dimensional bar with a discontinuity, i.e., a crack at $X=X^{\mathrm{c}}$ as shown in Fig. 2. The level set function f is considered negative and positive on the left and right sides of the crack, respectively. Fig. 2(a) illustrates an arbitrary displacement field consisting of two independent linear fields on each side of the crack. Such displacements can be reproduced by superimposing three independent parts: (i) a continuous displacement represented by the finite element interpolation shown in Fig. 2(b); (ii) a strong discontinuity represented by a jump in the displacement $[\![u]\!]$ at the non-nodal point at X^{c} as illustrated in Fig. 2(c); and (iii) a weak discontinuity represented by a jump in the strain $[\![L^e\nabla u]\!]$ at X^{c} as described in Fig. 2(d). Here, the element length L^e is consciously multiplied to make the units of nodal values consistent with other terms in (4). This results in significant reduction of the condition number of the stiffness matrix. Notice that four unknown variables are employed to approximate a displacement field in this bar, i.e., $\{u_1, u_2, [\![u]\!], [\![L^e\nabla u]\!]\}$.

Using these variables, the approximation of the displacement field in a one-dimensional bar can be defined by

$$\begin{aligned} u(X,t) &= u^{\mathrm{cont}}(X,t) + u^{\mathrm{disc}}(X,t) \\ &= \sum_{I=1}^{2} N_I(X)\,u_I(t) + \Psi^{\mathrm{u}}(X)\,[\![u(t)]\!] + \Psi^{\nabla \mathrm{u}}(X)\,[\![L^e\nabla u(t)]\!]. \end{aligned} \tag{4}$$

The non-nodal enrichment functions Ψ^{u} and $\Psi^{\nabla \mathrm{u}}$ are constructed so that (4) can reproduce the discontinuous displacement fields Φ^{u} and $\Phi^{\nabla \mathrm{u}}$ given in (2) and (3), respectively. These discontinuous fields are illustrated in Fig. 3.

Let us first consider the displacement field with a strong discontinuity, i.e., $u=\Phi^{\mathrm{u}}$. Then, the nodal values consisting of the regular and enriched degrees of freedom (DOFs) can be calculated as

$$\text{Regular DOFs}: \begin{cases} u_1 = 0 \\ u_2 = 1 \end{cases}, \qquad \text{Enriched DOFs}: \begin{cases} [\![u]\!] = 1 \\ [\![L^e\nabla u]\!] = 0. \end{cases}$$

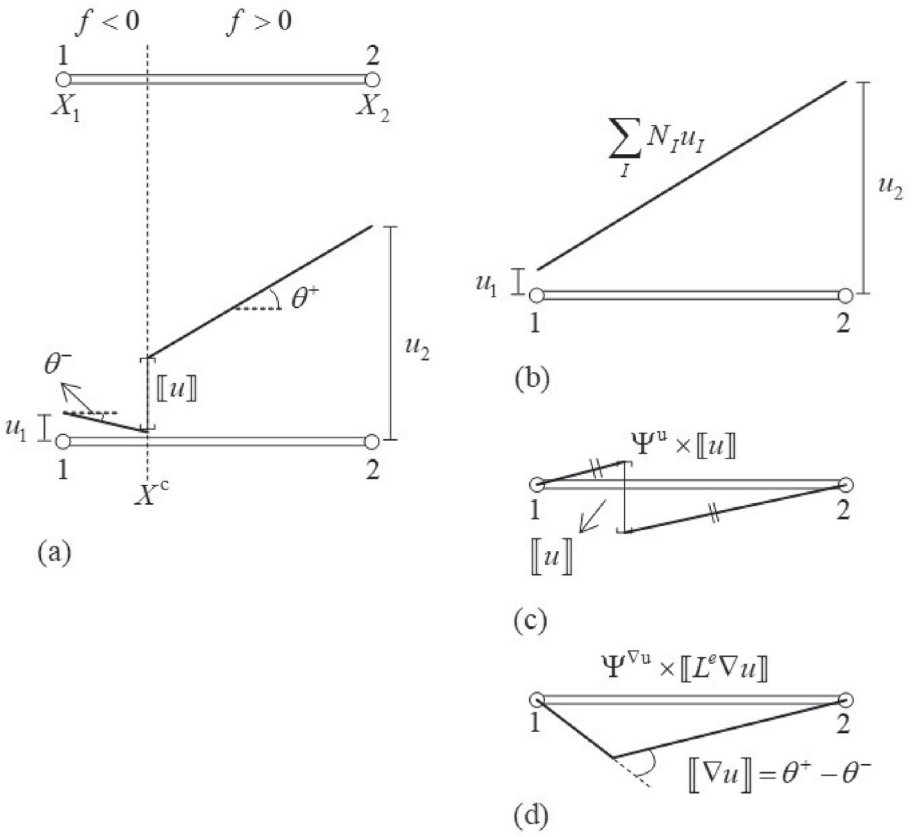

Fig. 2. One-dimensional enrichment displacement fields: (a) an arbitrary linear displacement field on both sides of the crack; (b) the finite-element displacement field u^{FEM}; (c) the enrichment displacement field produced by displacement jump enrichment $\Psi^{\mathrm{u}} \times [\![u]\!]$; and (d) the enrichment displacement field for gradient jump enrichment $\Psi^{\nabla \mathrm{u}} \times [\![L^e \nabla u]\!]$. Note that in one dimension for small derivatives $[\![\nabla u]\!] = [\![\epsilon]\!] = [\![\theta]\!] = \theta^+ - \theta^-$.

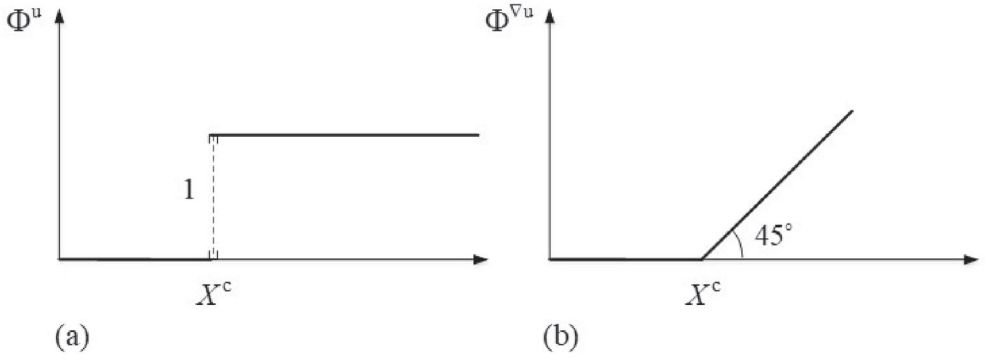

Fig. 3. Representation of the discontinuity in: (a) a function denoted by Φ^{u}; and (b) a derivative of a function denoted by $\Phi^{\nabla \mathrm{u}}$.

Substituting above values into (4), the enrichment function Ψ^{u} can be obtained as

$$\Psi^{\mathrm{u}} = \begin{cases} -N_2 & f < 0, \\ N_1 & f > 0. \end{cases} \tag{5}$$

Notice that since Φ^{u} introduces no discontinuity in strains, the enrichment parameter $[\![L^e \nabla u]\!]$ vanishes and consequently, the enrichment function Ψ^{u} is obtained identical to that in our previous study [22].

Similarly, considering a displacement field with a weak discontinuity, i.e., $u = \Phi^{\nabla \mathrm{u}}$, the nodal values can be obtained as

$$\text{Regular DOFs}: \begin{cases} u_1 = 0 \\ u_2 = X_2 - X^{\mathrm{c}} \end{cases}, \qquad \text{Enriched DOFs}: \begin{cases} [\![u]\!] = 0 \\ [\![L^e \nabla u]\!] = L^e. \end{cases}$$

Using these values, (4) can be expressed for each side of the crack as follows:

$$\begin{aligned} 0 &= N_2(X_2 - X^{\mathrm{c}}) + L^{\mathrm{e}} \Psi^{\nabla \mathrm{u}-}(X) \quad \text{if } f < 0, \\ X - X^{\mathrm{c}} &= N_2(X_2 - X^{\mathrm{c}}) + L^{\mathrm{e}} \Psi^{\nabla \mathrm{u}+}(X) \quad \text{if } f > 0. \end{aligned} \tag{6}$$

The linear term $X - X^{\mathrm{c}}$ can be interpolated exactly by the standard shape functions as $X - X^{\mathrm{c}} = \sum_{I=1}^{2} N_I (X_I - X^{\mathrm{c}})$, so (6) gives rise to the second enrichment function as follows:

$$\Psi^{\nabla \mathrm{u}} = \begin{cases} -s^+ N_2 & f < 0, \\ -s^- N_1 & f > 0, \end{cases} \tag{7}$$

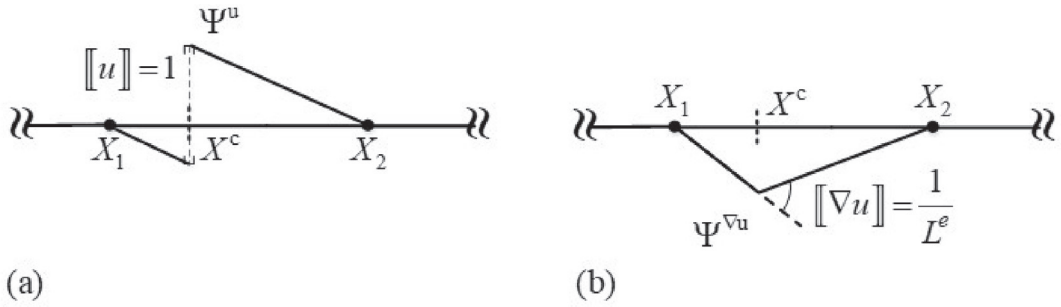

Fig. 4. One-dimensional crack enrichment functions: (a) Ψ^{u}; and (b) $\Psi^{\nabla u}$.

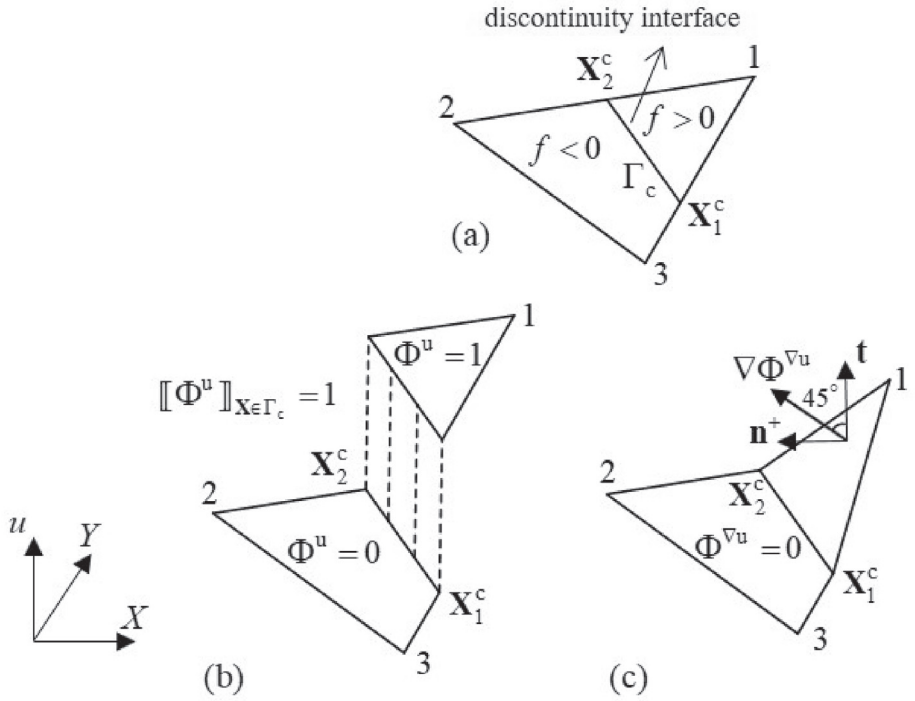

Fig. 5. A strong and weak discontinuity in two dimensions: (a) a triangular element with a crack; (b) Φ^{u}; and (c) $\Phi^{\nabla u}$.

in which s^+ and s^- are two normalized parameters indicating the ratios of the lengths of the left and right sides of the crack to the element length defined as

$$s^- = (X^c - X_1)/L^e, \qquad s^+ = (X_2 - X^c)/L^e.$$

These enrichment functions are illustrated in Fig. 4. Using these enrichment functions, the extended interpolation can reproduce two independent linear functions at both sides of the crack. The detailed proof is provided in Appendix A.

2.2. Representation of a crack with non-nodal enrichment parameters for three-node triangular elements

We consider a triangular element that is completely cut by a crack as shown in Fig. 5(a). For such a crack position, the strong and weak discontinuities given in (2) and (3) are illustrated in panels (b) and (c) of Fig. 5. The enrichment variables for capturing the strong discontinuity are chosen to be the displacement jumps at the intersection points of the crack and element edges, i.e., the displacement jumps at $\mathbf{X}_1^c$ and $\mathbf{X}_2^c$ denoted by $[\![u]\!]_1$ and $[\![u]\!]_2$, respectively.

The enrichment variables for capturing the weak discontinuity are selected to be the jumps in directional derivatives of the displacement at the intersection points. The ideal direction at a point on the interface could be the normal to the surface of the discontinuity. However, as in element-wise crack propagation, the crack direction changes at element edges, there are more than one normal to the crack surface at the intersection points. As a consequence, to satisfy the C^0-continuity condition, the directions of element edges, which are in common between adjacent elements, are chosen as the directions of derivatives. These directions are denoted by $\mathbf{e}_1^c$ and $\mathbf{e}_2^c$ and illustrated in Fig. 6. Notice that incorporating a finite element mesh into the definition of weak discontinuity enrichments can be attributed here to the element-wise crack propagation scheme.

The approximation of the displacement field $u(\mathbf{X})$ in a three-node triangular element can be given by

$$\begin{aligned} u(\mathbf{X}) &= u^{\text{cons}}(\mathbf{X}) + u^{\text{disc}}(\mathbf{X}) \\ &= \sum_{I=1}^{3} N_I(\mathbf{X}) u_I + \sum_{J\in\delta^u} \Psi_J^u(\mathbf{X}) [\![u]\!]_J + \sum_{K\in\delta^{\nabla u}} \Psi_K^{\nabla u}(\mathbf{X}) [\![L_K^c \nabla u \cdot \mathbf{e}_K^c]\!]_K, \end{aligned} \tag{8}$$

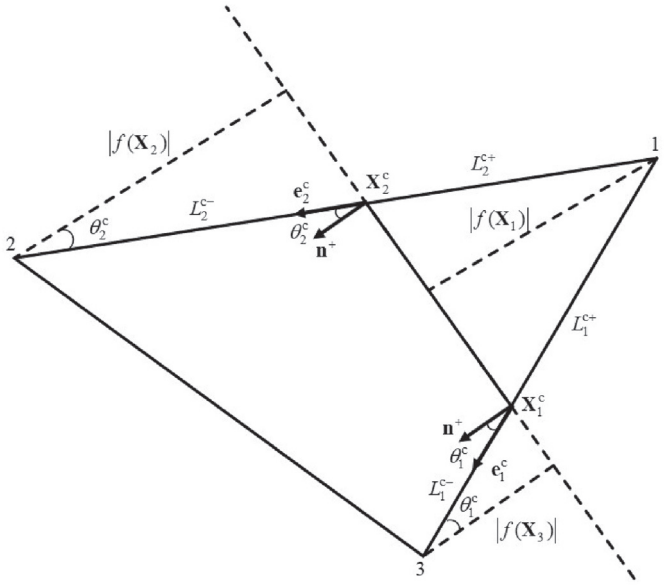

Fig. 6. Illustration of nomenclature for a linear complete non-nodal enrichment in two dimension.

in which δ^{u} and $\delta^{\nabla \mathrm{u}}$ are sets of non-nodal points on the interface, L_K^{c} is the length of an element edge that contains the points X_K^{c}, and $[\![\nabla u \cdot \mathbf{e}_K^{\mathrm{c}}]\!]_K$ is the jump in the directional derivative along $\mathbf{e}_K^{\mathrm{c}}$ at X_K^{c}. In the following, we consider a general case where the element is completely cut by a crack, i.e. $\delta^{\mathrm{u}} = \delta^{\nabla \mathrm{u}} = \{1, 2\}$.

Following the steps of the previous section, we first consider a displacement field including a strong discontinuity, i.e., $u = \Phi^{\mathrm{u}}$. For such a displacement field, the weak enrichment variables $[\![L_K^{\mathrm{c}} \nabla u \cdot \mathbf{e}_K^{\mathrm{c}}]\!]_K$ are vanished. This reduces to the interpolation in (8) to that in Ref. [22] and results in the identical enrichment functions as

$$\Psi_1^{\mathrm{u}} = \begin{cases} -\dfrac{N_1 \times N_3}{N_2 + N_3} & f < 0, \\ N_3 & f > 0, \end{cases} \quad \Psi_2^{\mathrm{u}} = \begin{cases} -\dfrac{N_1 \times N_2}{N_2 + N_3} & f < 0, \\ N_2 & f > 0. \end{cases} \tag{9}$$

Notice that the enrichment functions are defined to satisfy the C^0-continuity conditions between the enriched element and its contiguous elements (see Ref. [22] for more details). They can be also expressed in terms of four-node quadrilateral shape functions N^{4Q} as

$$\Psi_1^{\mathrm{u}} = \begin{cases} -N_1^{4Q} & f < 0, \\ N_4^{4Q} & f > 0, \end{cases} \quad \text{and} \quad \Psi_2^{\mathrm{u}} = \begin{cases} -N_2^{4Q} & f < 0, \\ N_3^{4Q} & f > 0. \end{cases} \tag{10}$$

Next, considering a displacement field with a weak discontinuity, i.e., $u = \Phi^{\nabla \mathrm{u}}$, the nodal values are determined as follows:

$$\text{Regular DOFs}: \begin{cases} u_1 = f(\mathbf{X}_1), \\ u_2 = 0, \\ u_3 = 0, \end{cases}$$

and

$$\text{Enriched DOFs}: \begin{cases} [\![u]\!]_1 = 0, \\ [\![L_1^{\mathrm{c}} \nabla u . \mathbf{e}_1^{\mathrm{c}}]\!]_1 = L_1^{\mathrm{c}} \dfrac{|f(\mathbf{X}_3)|}{L_1^{\mathrm{c}-}}, \\ [\![u]\!]_2 = 0, \\ [\![L_2^{\mathrm{c}} \nabla u . \mathbf{e}_2^{\mathrm{c}}]\!]_2 = L_2^{\mathrm{c}} \dfrac{|f(\mathbf{X}_2)|}{L_2^{\mathrm{c}-}}, \end{cases}$$

in which, for such a displacement, $\nabla u = \mathbf{n}^+ + \mathbf{t}$, as depicted in Fig. 5(c). By substituting above nodal values into the approximation (8) and rewriting it for each side of the interface, we have

$$f(\mathbf{X}) = N_1 f(\mathbf{X}_1) + \Psi_1^{\nabla \mathrm{u}+} L_1^{\mathrm{c}} \frac{|f(\mathbf{X}_3)|}{L_1^{\mathrm{c}-}} + \Psi_2^{\nabla \mathrm{u}+} L_2^{\mathrm{c}} \frac{|f(\mathbf{X}_2)|}{L_2^{\mathrm{c}-}},$$

$$0 = N_1 f(\mathbf{X}_1) + \Psi_1^{\nabla \mathrm{u}-} L_1^{\mathrm{c}} \frac{|f(\mathbf{X}_3)|}{L_1^{\mathrm{c}-}} + \Psi_2^{\nabla \mathrm{u}-} L_2^{\mathrm{c}} \frac{|f(\mathbf{X}_2)|}{L_2^{\mathrm{c}-}}.$$

Since the function f is a linear function, it can be exactly interpolated by standard shape functions as $f = \sum_{I=1}^{3} N_I f_I$. So, the enrichment functions $\Psi_1^{\nabla \mathrm{u}}$ and $\Psi_2^{\nabla \mathrm{u}}$ are obtained as

$$\Psi_1^{\nabla \mathrm{u}} = \begin{cases} -s_1^+ \dfrac{N_1 \times N_3}{N_2 + N_3} & f < 0, \\ -s_1^- N_3 & f > 0, \end{cases} \quad \Psi_2^{\nabla \mathrm{u}} = \begin{cases} -s_2^+ \dfrac{N_1 \times N_2}{N_2 + N_3} & f < 0, \\ -s_2^- N_2 & f > 0. \end{cases} \tag{11}$$

Here, we use the side-splitter theorem and define the normalized parameters $s_I^- = L_I^{\mathrm{c}-}/L_I^{\mathrm{c}}$ and $s_I^+ = L_I^{\mathrm{c}+}/L_I^{\mathrm{c}}$. They can also be expressed according to bilinear shape functions as

$$\Psi_1^{\nabla \mathrm{u}} = \begin{cases} -s_1^+ N_1^{4Q} & f < 0, \\ -s_1^- N_4^{4Q} & f > 0, \end{cases} \quad \text{and} \quad \Psi_2^{\nabla \mathrm{u}} = \begin{cases} -s_2^+ N_2^{4Q} & f < 0, \\ -s_2^- N_3^{4Q} & f > 0. \end{cases} \tag{12}$$

The strong and weak enrichment functions are illustrated in Fig. 7(a)–(d). Notice that, for a general crack position, the weak enrichment functions $\Psi^{\nabla \mathrm{u}}$ may introduce discontinuities across the interface. For an arbitrary discontinuity across the interface, the construction of non-nodal enrichment functions has been generalized for a multi-dimensional multi-node element in Ref. [22].

Enriching with Ψ^{u} and $\Psi^{\nabla \mathrm{u}}$ enables the approximation to reproduce two independent linear functions at either side of the crack shown in Fig. 7(e). The detailed proof has been provided in Appendix B.

3. Governing equations and discretization

3.1. Governing equations

The linear momentum equation in a total Lagrangian description is given by

$$\frac{\partial P_{ji}}{\partial X_j} + \rho b_i - \rho \ddot{u}_i = 0 \quad \text{in} \quad \Omega \tag{13}$$

where $\mathbf{P}$ is the nominal stress tensor, ρ is the initial density, and $\mathbf{b}$ is the body force vector per unit mass. The boundary conditions can be written as

$$\begin{aligned} u_i &= \overline{u}_i && \text{on} \quad \Gamma_{\mathrm{u}}, \\ [\![u]\!]_i &= [\![\overline{u}]\!]_i && \text{on} \quad \Gamma_{\mathrm{uc}}, \\ [\![\nabla u]\!]_i &= [\![\nabla \overline{u}]\!]_i && \text{on} \quad \Gamma_{\nabla \mathrm{uc}}, \\ n_j P_{ji} &= \overline{t}_i && \text{on} \quad \Gamma_{\mathrm{t}}, \\ n_j^{\pm} P_{ji}^{\pm} &= \tau_i^{\mathrm{c}}([\![u]\!]_i) && \text{on} \quad \Gamma_{\mathrm{c}}, \end{aligned} \tag{14}$$

in which $\overline{\mathbf{u}}$ is the prescribed displacement on the Dirichlet boundary Γ_{u}, $[\![\overline{\mathbf{u}}]\!]$ and $[\![\nabla \overline{\mathbf{u}}]\!]$ are the prescribed jumps in the displacement and its gradient on sets of non-nodal points located on Γ_{uc} and $\Gamma_{\nabla \mathrm{uc}}$, respectively. Here, τ^{c} is the cohesive traction on the crack surface, and $\overline{\mathbf{t}}$ is the prescribed traction on the Neumann boundary Γ_{t}. Superscripts plus and minus signs indicate two sides of the interface. The crack edge can be defined by imposing homogeneous prescribed displacement jumps as

$$[\![u]\!]_i = [\![\nabla u]\!]_i = 0 \quad \text{at crack edge.} \tag{15}$$

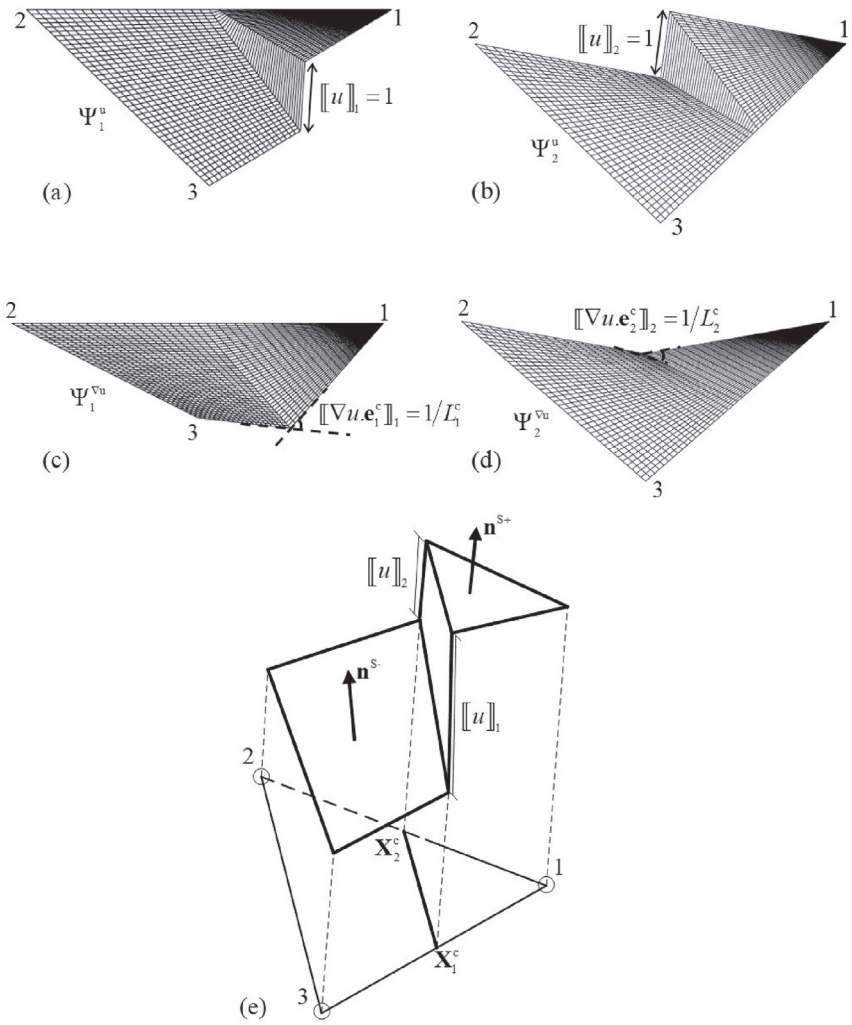

Fig. 7. The enrichment functions and their interpolated field: (a) Ψ_1^{u}; (b) Ψ_2^{u}; (c) $\Psi_1^{\nabla \mathrm{u}}$; (d) $\Psi_2^{\nabla \mathrm{u}}$; and (e) the representation of a discontinuity in a two-dimensional model. $\mathbf{n}^{\mathrm{S}+}$ and $\mathbf{n}^{\mathrm{S}-}$ are normal to the interpolation surfaces.

It is important to note that the essential boundary conditions on ∇u can be effectively adopted in modeling bi-material problems.

We define the spaces for the admissible displacement field $\mathbf{u}$ and the test field $\delta\mathbf{u}$ as

$$\mathscr{U} = \{\mathbf{u} \in \mathrm{C}^0 | \mathbf{u} = \overline{\mathbf{u}} \text{ on } \Gamma_{\mathrm{u}}, [\![\mathbf{u}]\!] = [\![\overline{\mathbf{u}}]\!] \text{ on } \Gamma_{\mathrm{uc}}, \mathbf{u} \text{ discontiniuous on } \Gamma_{\mathrm{c}}\},$$

$$\mathscr{U}_0 = \{\delta\mathbf{u} \in \mathrm{C} | \delta\mathbf{u} = 0 \text{ on } \Gamma_{\mathrm{u}}, [\![\delta\mathbf{u}]\!] = 0 \text{ on } \Gamma_{\mathrm{uc}}, \delta\mathbf{u} \text{ discontiniuous on } \Gamma_{\mathrm{c}}\}.$$

The weak form of (13) can be stated as: Find $\mathbf{u} \in \mathscr{U}$, for $\delta\mathbf{u} \in \mathscr{U}_0$,

$$\int_\Omega \delta\mathbf{u} \cdot \rho\ddot{\mathbf{u}} \mathrm{d}\Omega = \int_\Omega \delta\mathbf{u} \cdot \rho\mathbf{b} \mathrm{d}\Omega + \int_{\Gamma_{\mathrm{t}}} \delta\mathbf{u} \cdot \bar{\mathbf{t}} \mathrm{d}\Gamma_{\mathrm{t}} - \int_\Omega \delta\mathbf{F}^{\mathrm{T}} : \mathbf{P} \mathrm{d}\Omega - \int_{\Gamma_{\mathrm{c}}} [\![\delta\mathbf{u}]\!] \cdot \boldsymbol{\tau}^{\mathrm{c}} \mathrm{d}\Gamma_{\mathrm{c}} \tag{16}$$

where $\mathbf{F}$ is the deformation gradient.

3.2. Discretization

The weak form (16) is discretized by finite element discretization techniques yielding to

$$\int_{\Omega^e} \rho\mathbf{N}^{\mathrm{T}}\mathbf{N} \mathrm{d}\Omega^e \ddot{\mathbf{d}}_e = \int_{\Omega^e} \rho\mathbf{N}^{\mathrm{T}}\mathbf{b} \mathrm{d}\Omega^e + \int_{\Gamma_{\mathrm{t}}^e} \mathbf{N}^{\mathrm{T}}\bar{\mathbf{t}} \mathrm{d}\Gamma_{\mathrm{t}}^e - \int_{\Omega^e} \mathbf{B}^{\mathrm{T}}\mathbf{S} \mathrm{d}\Omega^e - \int_{\Gamma_{\mathrm{c}}^e} [\![\boldsymbol{\Psi}]\!]_e^{\mathrm{T}} \boldsymbol{\tau}^{\mathrm{c}} \mathbf{n} \mathrm{d}\Gamma_{\mathrm{c}}^e \tag{17}$$

where $\mathbf{S}$ is the second Piola-Kirchhoff stress in Voigt form and $\mathbf{d}_e$ is the generalized nodal coefficient matrix consisting of the nodal displacements and the enrichment parameters. It can be expanded for a triangular element as

$$\mathbf{d}_e = [\mathbf{u}_1,\ \mathbf{u}_2,\ \mathbf{u}_3,\ [\![\mathbf{u}]\!]_1,\ L_1^{\mathrm{c}}[\![\nabla\mathbf{u}.\mathbf{e}_1^{\mathrm{c}}]\!]_1,\ [\![\mathbf{u}]\!]_2,\ L_2^{\mathrm{c}}[\![\nabla\mathbf{u}.\mathbf{e}_2^{\mathrm{c}}]\!]_2]^{\mathrm{T}}. \tag{18}$$

The generalized shape function vector $\mathbf{N}$ is defined as

$$\mathbf{N} = [\mathbf{N}_1,\ \mathbf{N}_2,\ \mathbf{N}_3,\ \boldsymbol{\Psi}_1^{\mathrm{u}},\ \boldsymbol{\Psi}_1^{\nabla\mathrm{u}},\ \boldsymbol{\Psi}_2^{\mathrm{u}},\ \boldsymbol{\Psi}_2^{\nabla\mathrm{u}}]. \tag{19}$$

Similar to the steps in Ref. [23], the shape function derivative matrix associated to the node I is denoted by $\mathbf{B}_I$ and constructed as

$$\mathbf{B}_I = [\mathbf{B}_I^0,\ \mathbf{B}_I^{\mathrm{u}},\ \mathbf{B}_I^{\nabla\mathrm{u}}] \tag{20}$$

where

$$\mathbf{B}_I^0 = \begin{bmatrix} N_{I,\mathrm{X}}\, x_{,\mathrm{X}} & N_{I,\mathrm{X}}\, y_{,\mathrm{X}} \\ N_{I,\mathrm{Y}}\, x_{,\mathrm{Y}} & N_{I,\mathrm{Y}}\, y_{,\mathrm{Y}} \\ N_{I,\mathrm{X}}\, x_{,\mathrm{Y}} + N_{I,\mathrm{Y}}\, x_{,\mathrm{X}} & N_{I,\mathrm{X}}\, y_{,\mathrm{Y}} + N_{I,\mathrm{Y}}\, y_{,\mathrm{X}} \end{bmatrix},$$

$$\mathbf{B}_I^{\mathrm{u}} = \begin{bmatrix} \Psi_{I,\mathrm{X}}^{\mathrm{u}}\, x_{,\mathrm{X}} & \Psi_{I,\mathrm{X}}^{\mathrm{u}}\, y_{,\mathrm{X}} \\ \Psi_{I,\mathrm{Y}}^{\mathrm{u}}\, x_{,\mathrm{Y}} & \Psi_{I,\mathrm{Y}}^{\mathrm{u}}\, y_{,\mathrm{Y}} \\ \Psi_{I,\mathrm{X}}^{\mathrm{u}}\, x_{,\mathrm{Y}} + \Psi_{I,\mathrm{Y}}^{\mathrm{u}}\, x_{,\mathrm{X}} & \Psi_{I,\mathrm{X}}^{\mathrm{u}}\, y_{,\mathrm{Y}} + \Psi_{I,\mathrm{Y}}^{\mathrm{u}}\, y_{,\mathrm{X}} \end{bmatrix},$$

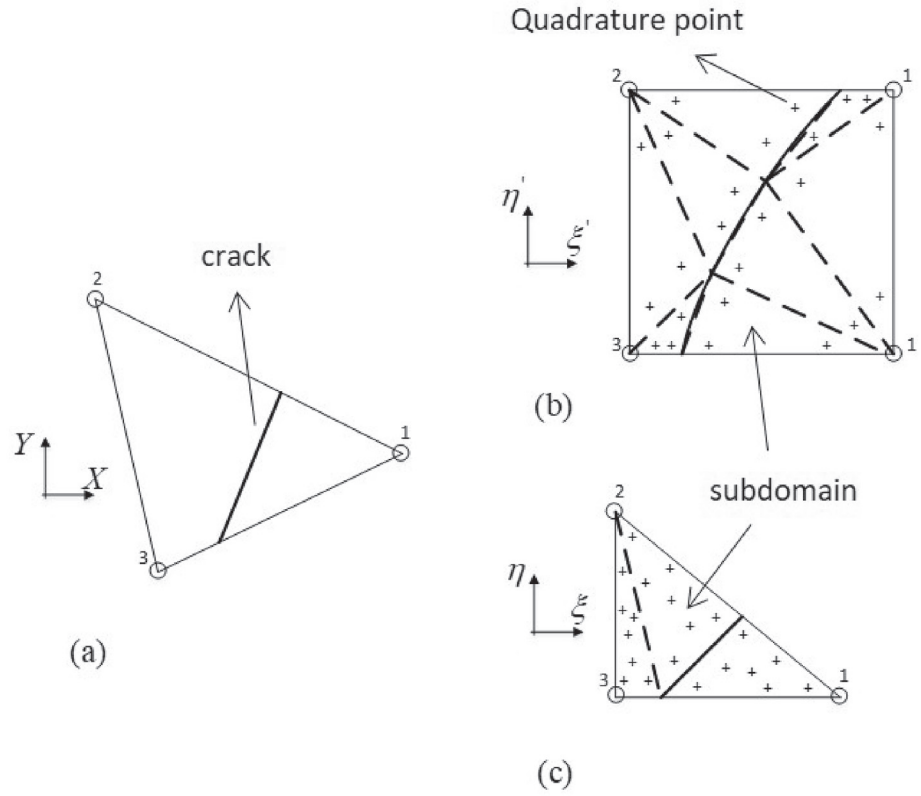

Fig. 8. Numerical integration with the subdomain integration schemes; (a) a cracked element in physical coordinates; (b) Duffy's parent domain; and (c) regular parent coordinates.

$$\mathbf{B}_I^{\nabla u} = \begin{bmatrix} \Psi_I^{\nabla u}{}_{,X}\, x_{,X} & \Psi_I^{\nabla u}{}_{,X}\, y_{,X} \\ \Psi_I^{\nabla u}{}_{,Y}\, x_{,Y} & \Psi_I^{\nabla u}{}_{,Y}\, y_{,Y} \\ \Psi_I^{\nabla u}{}_{,X}\, x_{,Y} + \Psi_I^{\nabla u}{}_{,Y}\, x_{,X} & \Psi_I^{\nabla u}{}_{,X}\, y_{,Y} + \Psi_I^{\nabla u}{}_{,Y}\, y_{,X} \end{bmatrix}.$$

Here, $(\cdot)_{,i}$ represents the partial derivative along the ith coordinate direction.

For the computation of the integrals in (17) within an enriched element where the integrands are discontinuous, a modified numerical quadrature scheme such as subdomain integration is used. In subdomain integration, the element domain is partitioned into several subdomains where the Gauss points are positioned as shown in Fig. 8(b)–(c). Here, we adopt two different subdomain integration schemes depending on the parent domains where the enrichment functions are defined. For the Duffy's parent domain, the enrichment functions are simply given in terms of bilinear shape functions as in (10) and (12). However, as a straight interface shown in Fig. 8(a) is mapped to a high curvature interface shown in Fig. 8(b), to maintain the accuracy of the integration, the interface is discretized, which leads to increased number of subdomains. For the standard parent domain shown in Fig. 8(c), the enrichment functions are given in (9) and (11). Since these enrichment functions are non-polynomial functions, higher number of Gauss points are required to maintain the integration accuracy.

3.3. Time stepping algorithm

We employ the explicit central difference time-stepping algorithm [23] which is conditionally stable, i.e., it is stable when

$$\Delta t \le \Delta t_c = \frac{2}{\omega_{\max}}. \tag{21}$$

By studying the frequencies ω_i of the one-dimensional discrete system $\omega_i^2 \mathbf{M}\mathbf{d}_i = \mathbf{K}\mathbf{d}_i$, the variation of the critical time step size according to the normalized location of the crack is pre-determined. Fig. 9 compares the normalized critical time step size of three methods: (a) a standard XFEM; (b) a non-nodal XFEM with only strong enrichment functions Ψ^u introduced in Ref. [22]; and (c) the proposed method, i.e., the non-nodal XFEM with both strong and weak enrichment functions.

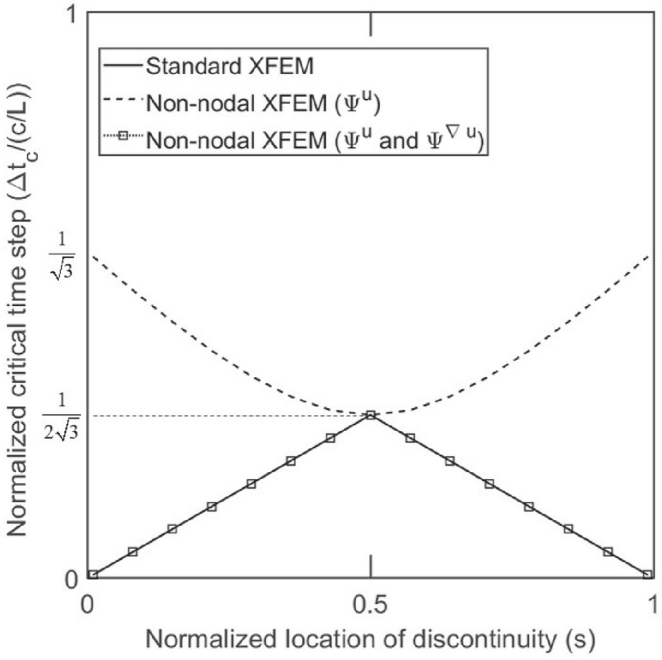

Fig. 9. The variation of the normalized critical time step size according to the normalized location of the discontinuity.

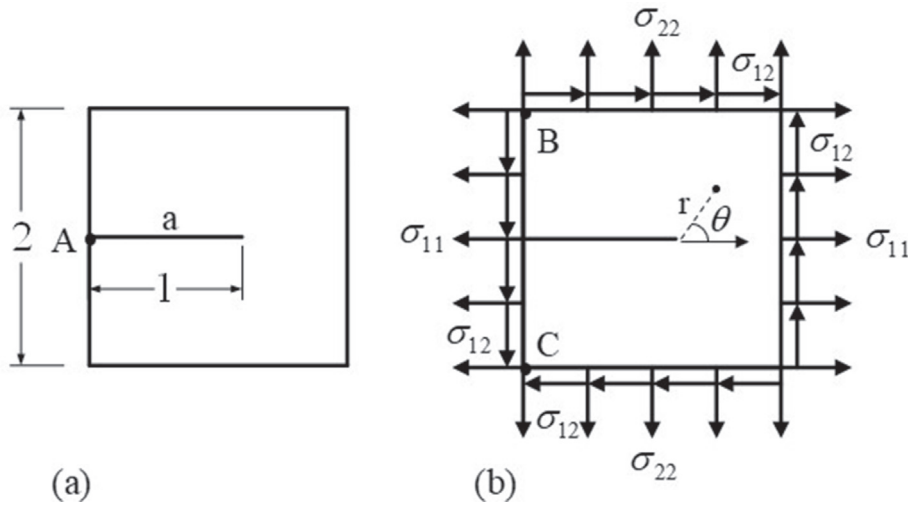

Fig. 10. A square patch for the near-tip crack problem: (a) geometry; and (b) boundary conditions.

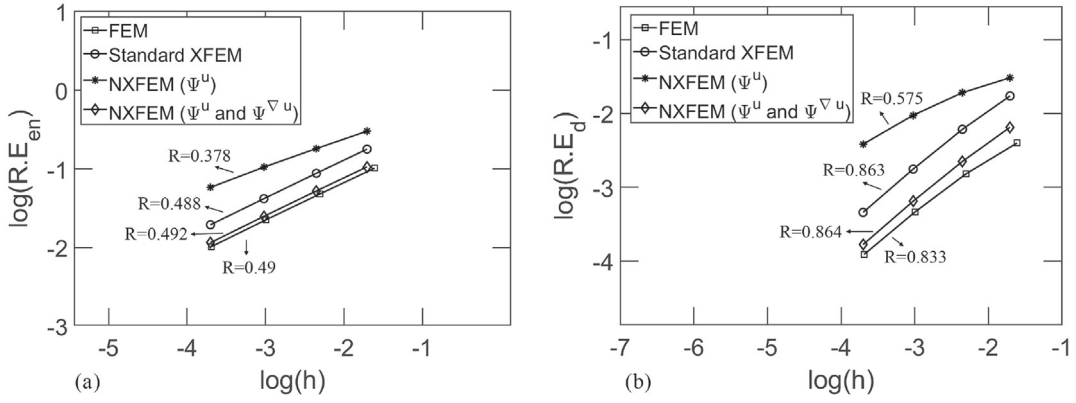

Fig. 11. Convergence study for the near-tip crack problem: (a) Energy-norm errors; and (b) L^2-norm errors.

As it can be seen from Fig. 9, the critical time size for the proposed method is identical to that of the standard XFEM; its peak occurs when the crack is in the middle of the element and it drops linearly to zero as the crack location approaches to the element nodes. This implies that the zero critical time step sizes can be attributed to capturing discontinuities in strains because it would not occur for the non-nodal XFEM with only strong enrichment functions. To avoid the zero critical time step sizes, we do not allow the ratio of the area of the smaller side of the crack $A_{\min}$ to the area of the element A to be less than 0.1, i.e., $A_{\min}/A > 0.1$ (see Ref. [4] for more details).

3.4. Cohesive law

In this study, a linear cohesive model is used for the damage evolution created by the crack. A cohesive model is usually applied to the crack surfaces to balance the energy dissipated due to the crack evolution and the critical fracture energy. Since the mode I is a dominant failure mode of the subsequently described failure problems, we consider only the normal component of the cohesive traction, which can be written in terms of the normal displacement jump δ_N defined by

$$\delta_N = \mathbf{n}\cdot[\![\mathbf{u}]\!] = \mathbf{n}\cdot\left(\sum_{J\in\delta^{\mathrm{u}}}[\![\boldsymbol{\Psi}_J^{\mathrm{u}}]\!][\![\mathbf{u}]\!]_J + \sum_{K\in\delta^{\nabla\mathrm{u}}}[\![\boldsymbol{\Psi}_K^{\nabla\mathrm{u}}]\!][\![L_K^{\mathrm{c}}\nabla\mathbf{u}\cdot\mathbf{e}_K^{\mathrm{c}}]\!]_K\right). \quad (22)$$

It must be stressed out that the derivative enrichment functions $\Psi^{\nabla u}$ are not in general continuous across the interface. So, they contribute to cohesive force computations. The cohesive traction is computed using a radial-return algorithm in Ref. [22].

4. Numerical study

The capability of the proposed method is tested for both static and dynamic problems. In the first two examples, the convergence of the proposed method is verified through static problems from linear elastic fracture mechanics. Moreover, we consider two benchmark problems with experimental results to validate the method for modeling dynamic crack propagation.

To effectively demonstrate the benefits of the method, we solve the problems using three approaches: (i) a standard XFEM, (ii) a non-nodal XFEM considering only strong enrichment functions Ψ^{u} as in Ref. [22], and (iii) the proposed linear complete non-nodal XFEM. We denote by NXFEM in the figure legends for a non-nodal XFEM. The central difference method for time integration is used with a Courant number of 0.1. All simulations are solved using constant strain triangular elements, plane strain, and thicknesses of unity. The fracture criterion used in this study is the maximum tensile stress computed at the crack front. The direction of the crack is selected to be normal to the maximum tensile stress direction. To eliminate awkward oscillations in stress computation, once an element failed, the stresses about the crack edge are averaged using nodal smoothing techniques.

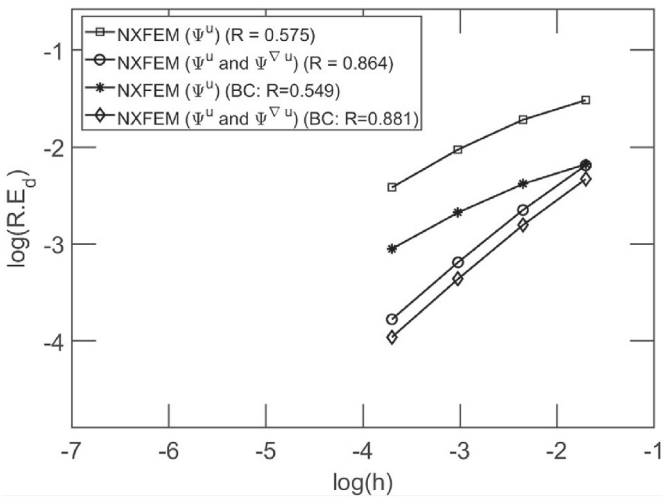

Fig. 12. Comparison of rates of convergence in L^2-norm errors of the near-tip crack problem for non-nodal XFEM with and without Dirichlet boundary conditions on the interface.

The relative errors in the energy norm denoted by $R.E_{\text{en}}$ and L^2-norm denoted by $R.E_{\text{d}}$ used in the analysis are defined as

$$(R.E_{\text{en}})^2 = \frac{\int_\Omega (\boldsymbol{\varepsilon} - \boldsymbol{\varepsilon}^{\text{h}})^{\text{T}} \mathbf{C} (\boldsymbol{\varepsilon} - \boldsymbol{\varepsilon}^{\text{h}})\, \text{d}\Omega}{\int_\Omega \boldsymbol{\varepsilon}^{\text{T}} \mathbf{C} \boldsymbol{\varepsilon}\, \text{d}\Omega}, \quad (R.E_{\text{d}})^2 = \frac{\int_\Omega (\mathbf{u} - \mathbf{u}^{\text{h}})^2\, \text{d}\Omega}{\int_\Omega \mathbf{u}^2\, \text{d}\Omega}.$$

4.1. Near-tip crack field

To demonstrate the capability of the proposed method for reproducing non-smooth solutions, a square patch with the same length and height $L = H = 2$ and a crack length $a = H/2 = 1$ is considered as shown in Fig. 10.

Tractions are prescribed along the boundary and the rigid body motions are avoided by prescribing displacements at nodes B and C as shown in Fig. 10(b). The closed-form stress fields ahead of a crack tip for the mode I in polar coordinates (r, θ) are given by

$$\sigma_{11}(r,\theta) = \frac{K_I}{\sqrt{2\pi r}} \cos\frac{\theta}{2}\left(1 - \sin\frac{\theta}{2}\sin\frac{3\theta}{2}\right),$$

$$\sigma_{22}(r,\theta) = \frac{K_I}{\sqrt{2\pi r}} \cos\frac{\theta}{2}\left(1 + \sin\frac{\theta}{2}\sin\frac{3\theta}{2}\right),$$

$$\sigma_{12}(r,\theta) = \frac{K_I}{\sqrt{2\pi r}} \cos\frac{\theta}{2}\sin\frac{\theta}{2}\cos\frac{3\theta}{2}.$$

The closed-form displacement fields are also given by

$$u_1(r,\theta) = \frac{K_I}{2\mu}\sqrt{\frac{r}{2\pi}}\cos\frac{\theta}{2}\left(k - 1 + 2\sin^2\frac{\theta}{2}\right),$$

$$u_2(r,\theta) = \frac{K_I}{2\mu}\sqrt{\frac{r}{2\pi}}\sin\frac{\theta}{2}\left(k + 1 - 2\cos^2\frac{\theta}{2}\right),$$

where μ is the shear modulus and k is the Kolosov constant defined as

$$k = \begin{cases} 3 - 4\nu & \text{(plane strain)}, \\ \dfrac{3-\nu}{1+\nu} & \text{(plane stress)}. \end{cases}$$

The material properties selected are: Young's modulus $E = 10^5$ and Poisson's ratio $\nu = 0.3$. The stress intensity factor is prescribed as $K_I = 1.0$.

A convergence study is carried out using structured linear triangular elements. Plots of errors in both energy norm and L^2-norm are provided in Fig. 11. The rates of convergence in the energy norm for the regular FEM, the standard XFEM, and the proposed method are around 0.49 which is very close to the optimal value of 0.5. Notice that the convergence rate in the energy norm for the non-smooth crack-tip problem is $O(h^{1/2})$ as indicated in Refs. [24,25].

Moreover, the results demonstrate that the proposed method outperforms the standard XFEM as the graph shows a constant shift toward lower error. Also, the non-nodal XFEM (NXFEM) with only Ψ^u enrichment as in Ref. [22] underperforms the other XFEM schemes but its convergence rate improves with mesh refinement as it is illustrated from L^2-norm results in Fig. 11(b).

One advantage of the proposed method is to improve accuracy by imposing Dirichlet boundary conditions on the interface. In doing so, closed-form displacement jumps are imposed at the non-nodal point on the left edge, i.e., point A in Fig. 10. These constraints can be expressed as

$$[\![\overline{u}_A]\!]_X = 0, \qquad [\![\overline{u}_A]\!]_Y = -2\,u_2(1,\pi).$$

The convergence results in L^2-norm are displayed in Fig. 12. With Dirichlet boundary conditions imposed on the interface, relatively lower errors are observed for both non-nodal XFEM schemes, indicating the improvement of accuracy of our method. Moreover, these boundary conditions lead to the rate of convergence of R = 0.881 which is a slightly better convergence rate of the proposed method than the

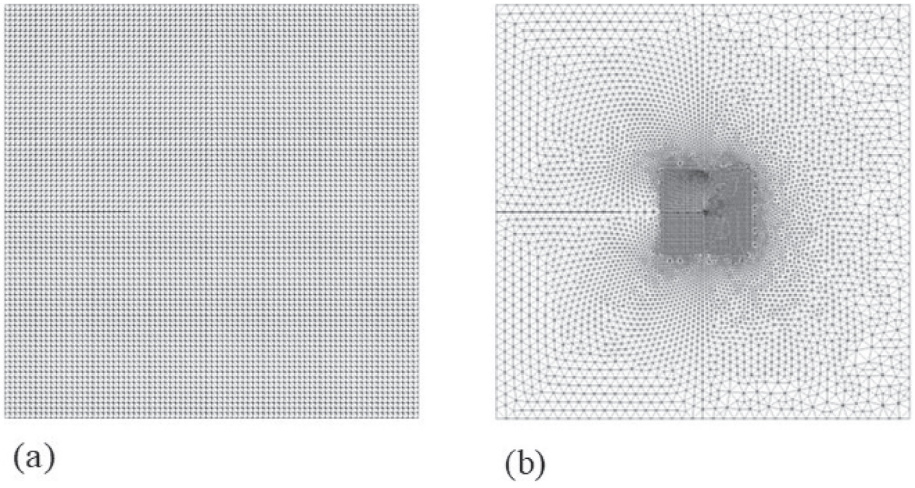

Fig. 13. Mesh models used for the stress convergence of the near-tip crack problem: (a) an 80×80 structured mesh; and (b) a refined mesh with around 13000 elements.

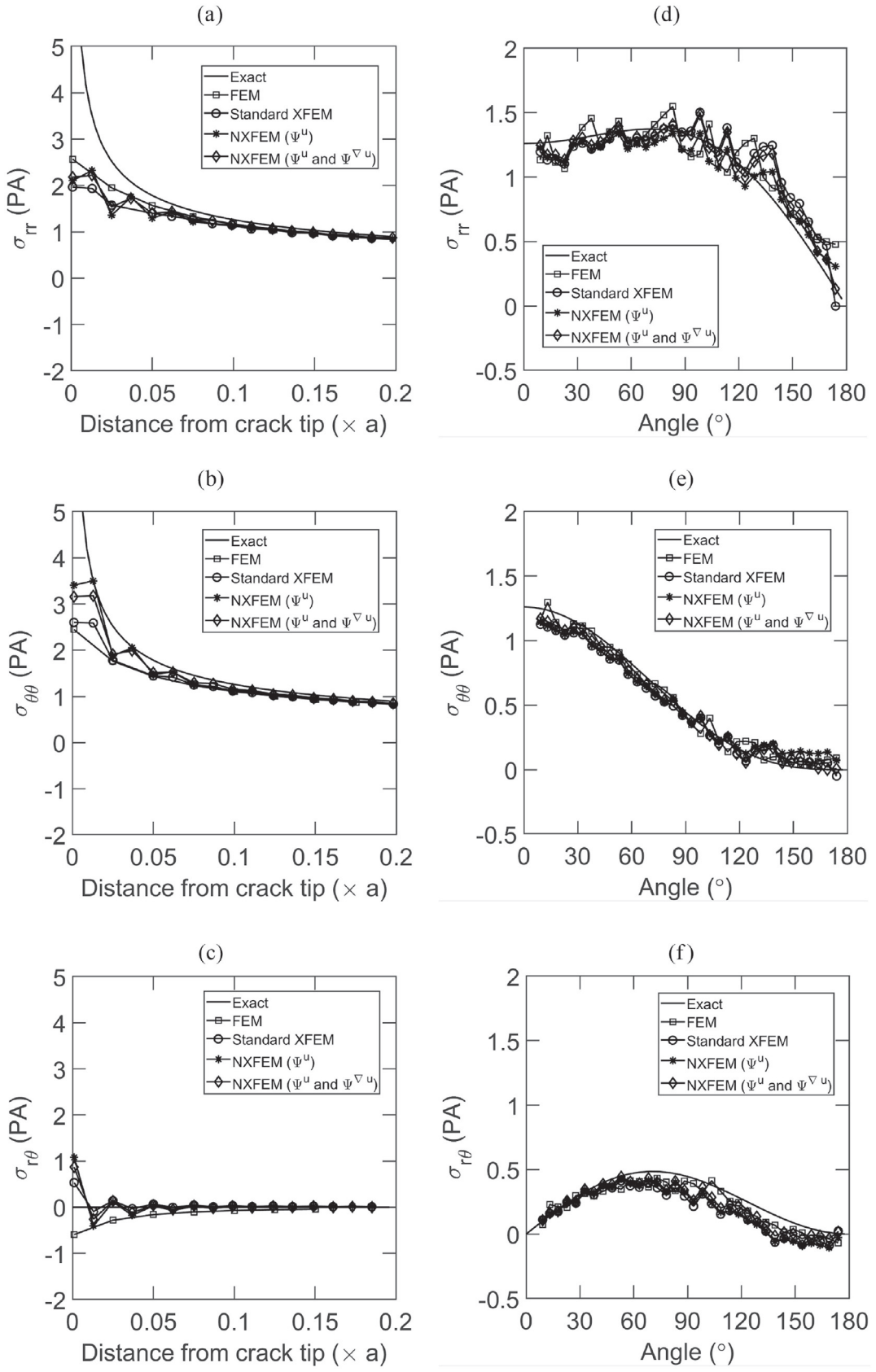

Fig. 14. Stresses of the near-tip crack problem for the 80 × 80 structured mesh: (a–c) ahead of the crack tip; (d–f) angular variation along constant radius ($r = 0.1a$).

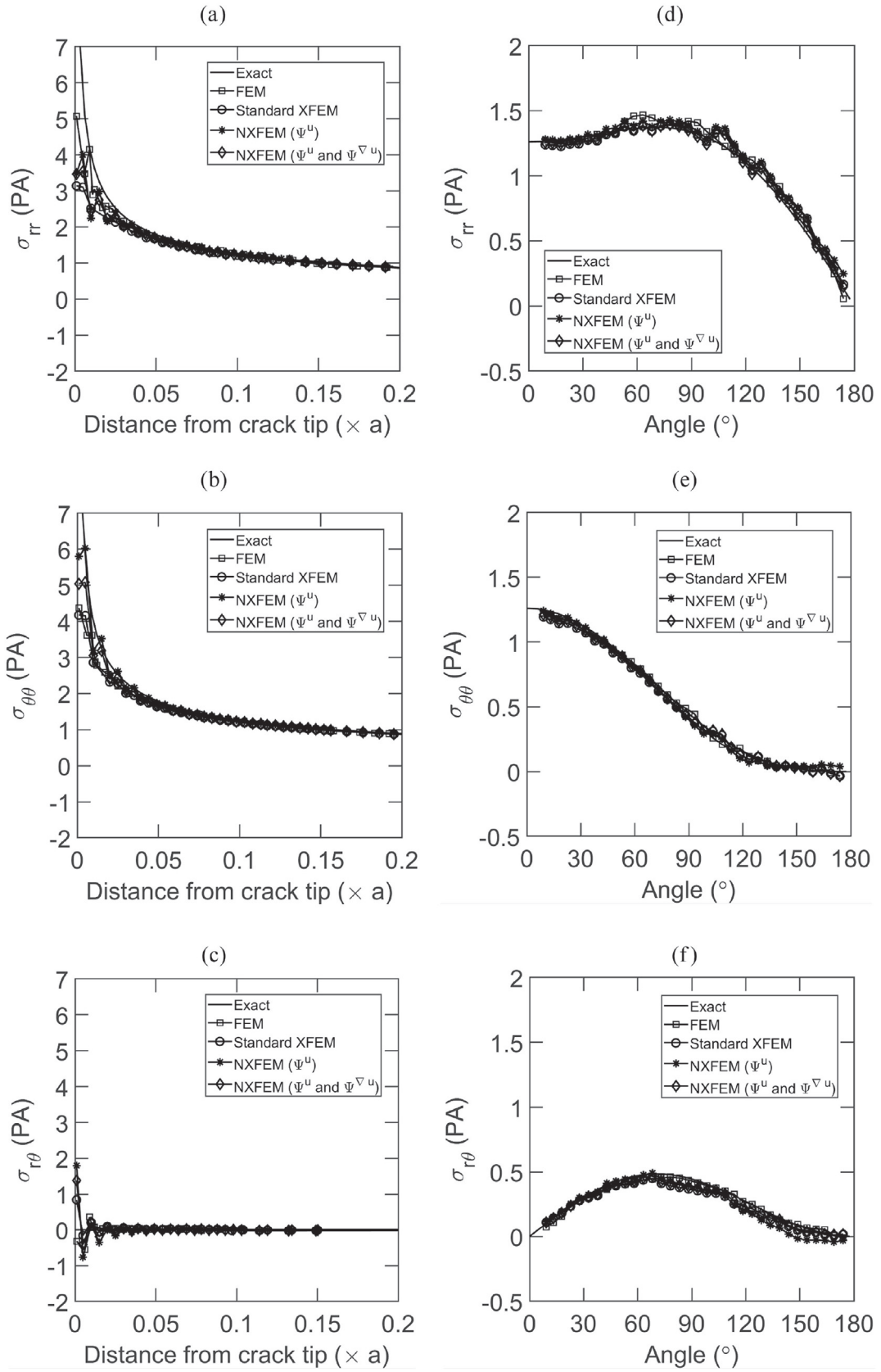

Fig. 15. Stresses of the near-tip crack problem for the refined mesh: (a–c) ahead of the crack tip; (d–f) angular variation along constant radius ($r = 0.1a$).

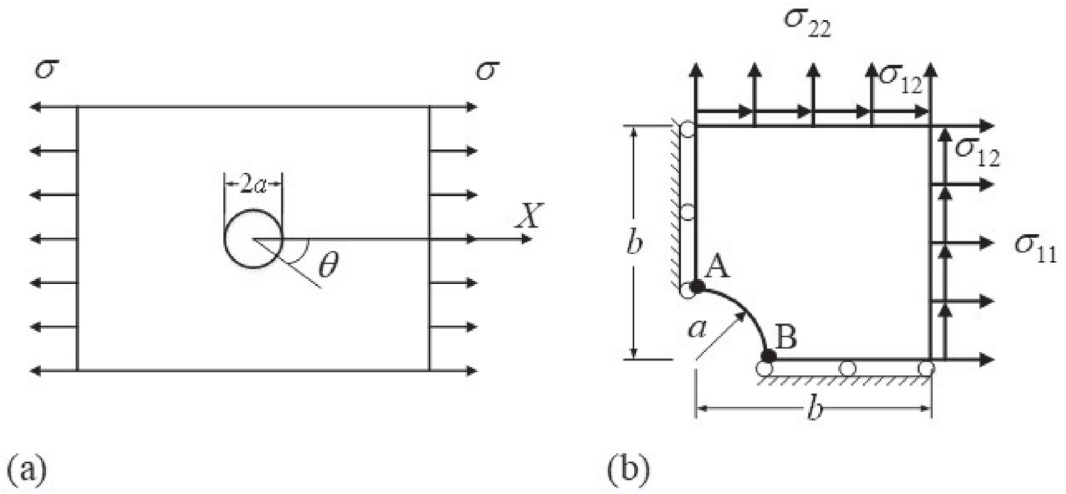

Fig. 16. (a) Infinite plate with a circular hole subjected to uniform tension; and (b) upper right quadrant of a square of edge length 2b centered at (0, 0) is modeled due to symmetry.

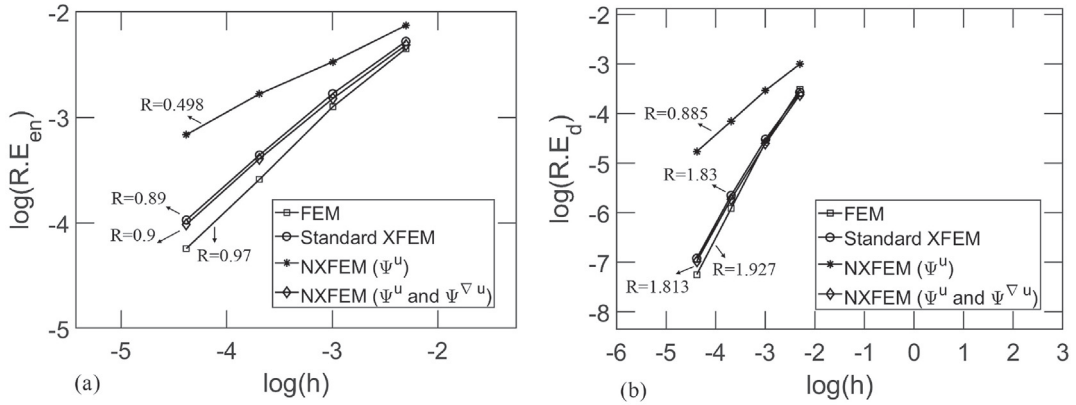

Fig. 17. Convergence study for the plate with a circular hole at the center for four enrichment schemes: (a) Energy-norm errors; and (b) *L*2-norm errors.

one (i.e., R = 0.864) obtained from the previous study without imposing Dirichlet boundary conditions.

The stresses are compared with exact solutions using both an 80 × 80 structured mesh and a refined mesh near the crack tip as shown in Fig. 13. The stresses computed along $\theta = 0$ from the crack tip are shown in Fig. 14(a)–(c) for the structured mesh and Fig. 15(a)–(c) for the refined mesh. Also, the angular variation of stresses at $r = 0.1$a from the crack edge are shown in Fig. 14(d)–(f) for the structure mesh and Fig. 15(d)–(f) for the refined mesh. As shown in the figures, the stresses oscillate near the crack tip for both mesh types. The singularity at the crack tip also has not been captured. This is expected because we have not introduced any enrichment functions to capture the near-tip singu-

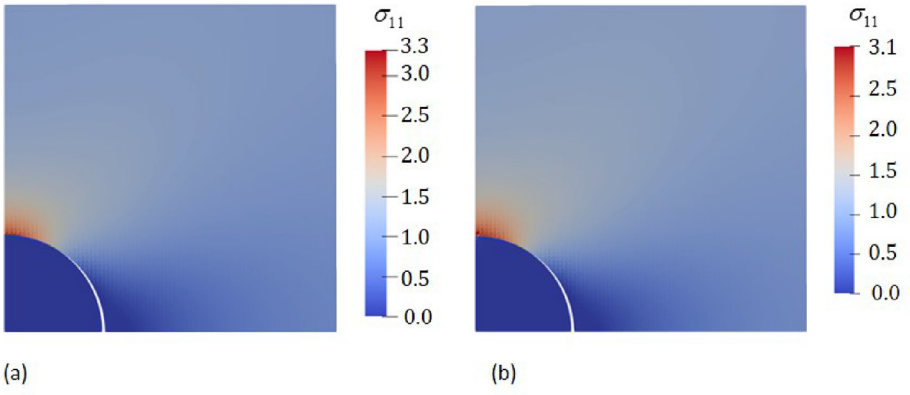

Fig. 18. Contour plots of the normal stress σ_{11} in deformed configuration (×1000): (a) the proposed method and the standard XFEM; and (b) the proposed method with interface constrains.

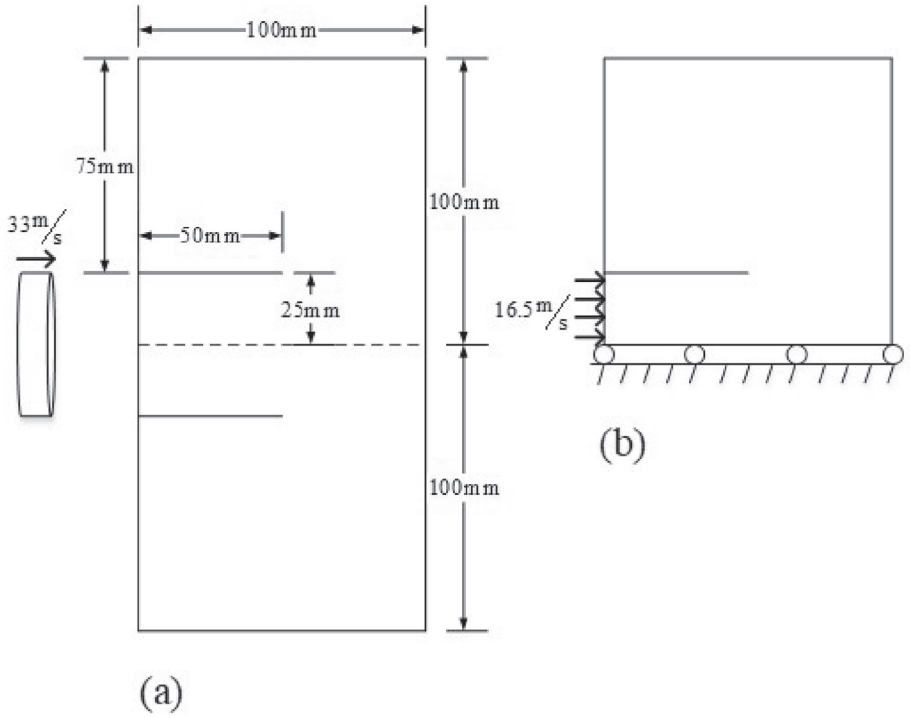

Fig. 19. (a) Kalthoff experimental set-up under impulsive loading; and (b) upper half of the plate analyzed dye to twofold symmetry.

lar fields. However, with mesh refinement, the computed stresses converge to the closed-form solutions.

4.2. Stress concentration in an infinite plate with a circular hole

To demonstrate the performance of the proposed method for modeling of discontinuities in strains, an infinite plate with a small circular hole of radius a subjected to uniform tension σ along X direction is considered (see Fig. 16(a)). Since the exact solution is given for the region close to the circle [26], we consider a square domain of edge length $2b$ with the circular hole at its center as in Ref. [27]. To take advantage of symmetry, only the upper right quadrant is considered as shown in Fig. 16(b). The symmetric constraints are imposed on bottom and left edges; the exact tractions are imposed on top and right edges. The closed-form solutions for the stress distribution in polar coordinates (r, θ) are given by

$$\sigma_{11}(r,\theta) = \sigma\left[1 - \frac{a^2}{r^2}\left(\frac{3}{2}\cos 2\theta + \cos 4\theta\right) + \frac{3}{2}\frac{a^4}{r^4}\cos 4\theta\right],$$

$$\sigma_{22}(r,\theta) = \sigma\left[-\frac{a^2}{r^2}\left(\frac{1}{2}\cos 2\theta - \cos 4\theta\right) - \frac{3}{2}\frac{a^4}{r^4}\cos 4\theta\right],$$

$$\sigma_{12}(r,\theta) = \sigma\left[-\frac{a^2}{r^2}\left(\frac{1}{2}\sin 2\theta + \sin 4\theta\right) + \frac{3}{2}\frac{a^4}{r^4}\sin 4\theta\right].$$

The closed-form displacements are given by

$$u_1(r,\theta) = \frac{a\sigma}{8\mu}\left[\frac{r}{a}(k+1)\cos\theta + 2\frac{a}{r}((1+k)\cos\theta + \cos 3\theta) - 2\frac{a^3}{r^3}\cos 3\theta\right],$$

$$u_2(r,\theta) = \frac{a\sigma}{8\mu}\left[\frac{r}{a}(k-3)\sin\theta + 2\frac{a}{r}((1-k)\sin\theta + \sin 3\theta) - 2\frac{a^3}{r^3}\sin 3\theta\right].$$

We take Young's modulus $E = 10^5$ and Poisson's ratio $\nu = 0.3$. The analyses are performed considering the following parameters: $\sigma = 1$, $a = 0.3$, and $b = 1$. In Fig. 17, a convergence study is conducted using linear triangular elements. The convergence rates were resulted slightly sub-optimal for both the standard XFEM and the proposed method. Notice that the optimal convergence rates for energy norm and L^2-norm are 1.0 and 2.0, respectively [27]. The proposed method obtains convergence rates of 0.9 and 1.813 in the energy norm and L^2-norm, respectively. However, the method presented in Ref. [22] gives the convergence rates of 0.498 and 0.885. This is expected because the enrichment function Ψ^u can only capture strong discontinuities while there is a weak discontinuity inside elements in this problem.

Contour plots for the normal stress σ_{11} are shown in Fig. 18. Fig. 18(a) shows that the maximum normal stress for both standard XFEM and the proposed method is 3.3 which is more than the theoretical value of 3.0. To improve the accuracy of the results, two Dirichlet boundary conditions on left and bottom edges are imposed to the displacement jumps on the intersection points of the circular hole and square edges, i.e., points A and B in Fig. 16. These constraints can be expressed as

$$[\![\overline{u}_A]\!]_X = 0, \quad [\![\overline{u}_B]\!]_Y = 0$$

The resulted normal stresses are shown in Fig. 18(b). As it can be seen, the maximum normal stress is 3.1, which is very closed to the theoretical value.

4.3. Edge-cracked plate under impulsive loading

This numerical example concerns a plate with two initial edge notches whose experiment carried out by Kalthoff and Winkler [28]. The plate is subjected to a projectile with different impact velocities which can be modeled as prescribed boundary conditions. Based on numerical observations, the impact velocity directly determines the failure pattern so that at lower velocities a brittle fracture with a crack propagation at an angle of about 70° was observed while a shear band was detected at higher velocities.

In this work, we consider only the brittle fracture mode. Numerical results for this problem can be found in Refs. [8,10]. The experimental set-up and the upper half of the plate which is analyzed due to two-fold

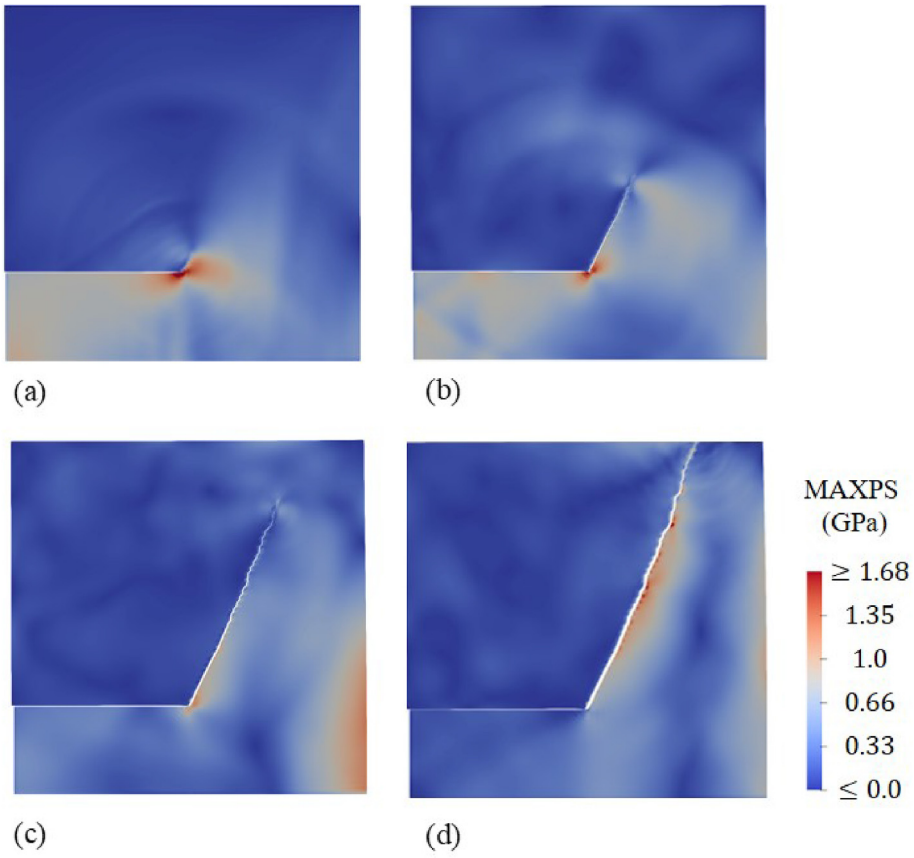

Fig. 20. The computed crack paths using linear complete formulations on the 120 × 120 deformed mesh with a maximum principle stress at different time steps: (a) $t = 25.72\,\mu s$; (b) $t = 38.22\,\mu s$; (c) $t = 56.54\,\mu s$; and (d) $t = 78.68\,\mu s$.

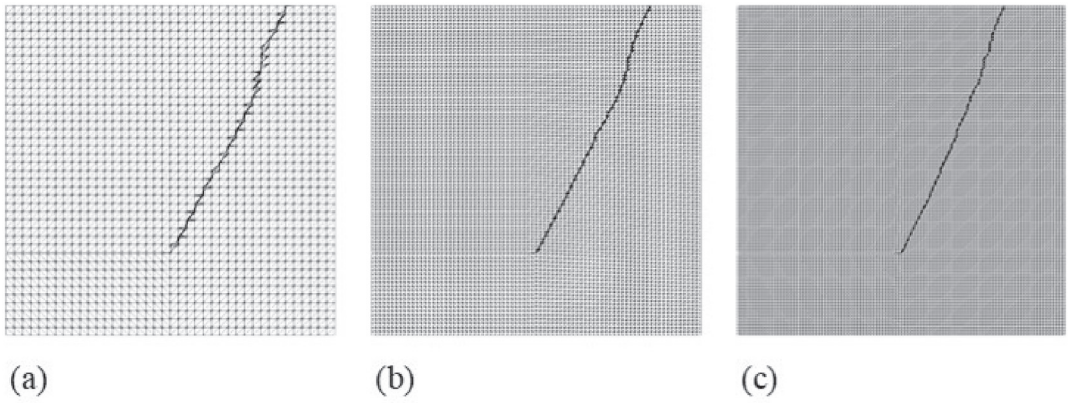

Fig. 21. Comparison of crack propagation trajectories using linear complete formulation at final simulation step using triangular linear elements (a) 40 × 40 mesh; (b) 80 × 80 mesh; and (c) 120 × 120 mesh.

symmetry are shown in Fig. 19. Considering the same elastic impedance for the projectile and the plate material, a velocity of 16.5 m/s is chosen.

The material parameters are: $\rho = 8000\,kg/m^3$, $E = 190\,GPa$, and $\nu = 0.3$; they lead to a Rayleigh wave speed of about $C_R = 2800\,m/s$. A linear cohesive crack model with fracture energy $G_F = 2.213 \times 10^4\,N/m$ and a critical crack opening displacement $\delta_{max} = 5.245 \times 10^{-5}\,m$ with a tensile strength of $\tau_{max} = 844\,MPa$ are used.

To observe the mesh sensitivity, we study the crack evolutions for 40 × 40, 80 × 80 and 120 × 120 meshes. In Fig. 20, the crack paths on different crack-tip speeds are displayed for only 120 × 120 mesh. Notice that similar results are observed for both 40 × 40 and 80 × 80 meshes. Plots of the crack propagation trajectories obtained from all three mesh types are presented in Fig. 21. All simulation results show similar crack

Table 1
Crack propagation angles and timing data using linear complete formulation for the Kalthoff's experiment.

Mesh	Angles(°)		Time(μs)	
	Initial	Overall	Propagation	Simulation
40 × 40	61.63	64.63	25.55	82.85
80 × 80	63.02	65.88	22.50	78.43
120 × 120	65.18	68.77	19.7	77.4

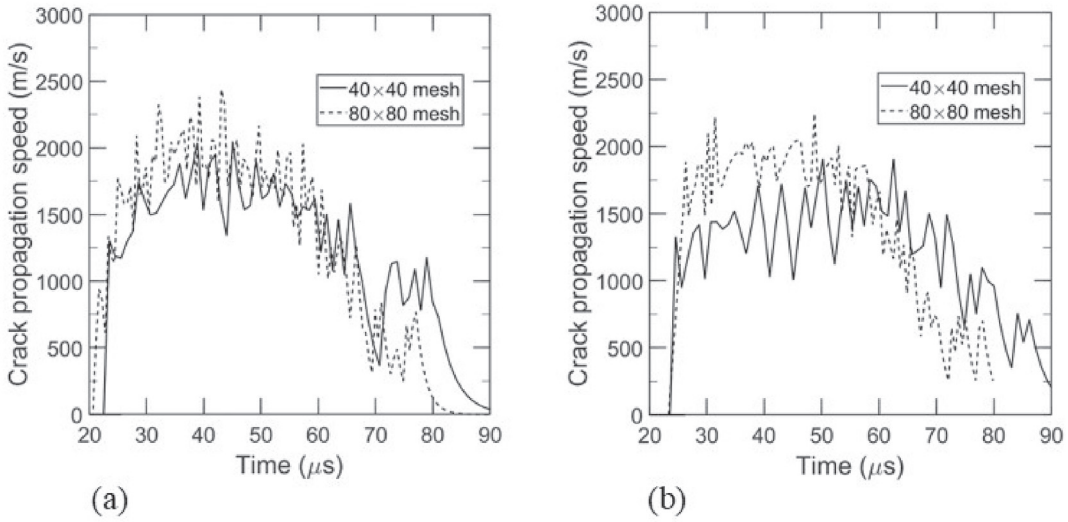

Fig. 22. Crack speeds for the Kolthoff's experiment simulation: (a) the crack speed of linear complete formulation and (b) the crack speed of the standard XFEM.

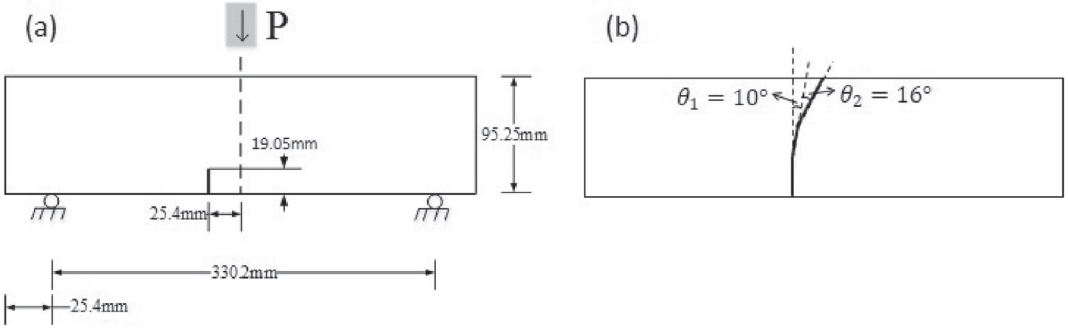

Fig. 23. A three-point bend test: (a) the geometry and boundary conditions; and (b) the experimentally obtained crack path.

paths which agree well with those reported by experiments [28] and the other XFEM schemes [8,10]. More details for each simulation are listed in Table 1. The data in Table 1 shows that the overall crack propagation angle approaches to the experimentally obtained value of 70° with mesh refinement. This angle is slightly bigger than the angle reported in Ref. [22]. The difference may be resulted from capturing the independent linear displacements in the presented work which yields to predict the strains more accurately.

The crack tip propagation speeds for 40×40 and 80×80 meshes are shown in Fig. 22. For the proposed method, Fig. 22(a) displays slightly faster speed for 80×80 mesh than 40×40 mesh. The crack speed increases up to 2000m/s and 2500 m/s for 40×40 and 80×80, respectively. For both simulations, after 45 μs, the crack tip speed decreases up to the end of the simulation. However, for the conventional XFEM result shown in Fig. 22(b), there is a significant difference in the crack speeds for different meshes. These results indicate that the proposed method is less sensitive to the mesh than the conventional XFEM.

4.4. Crack extension and velocity in three-point bending specimens

In this section, we apply our method to a three-point bend specimen problem reported by Guo et al. [29]. Ruiz et al. [30] modeled this

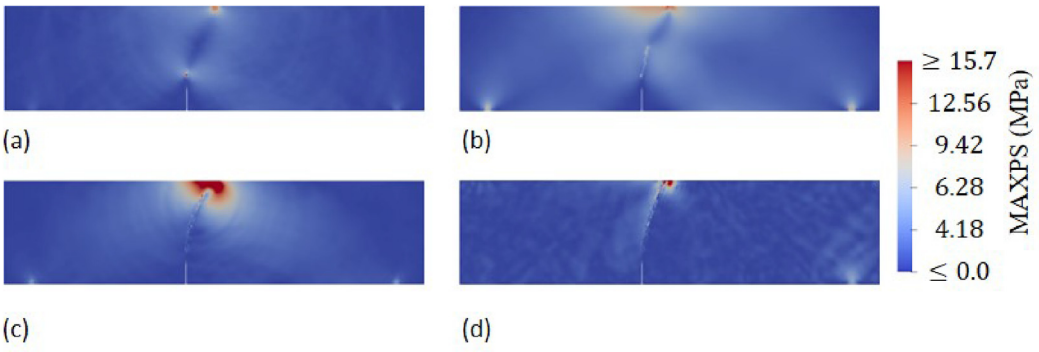

Fig. 24. The crack evolution resulted from linear complete enriched formulation for fine mesh: (a) $t=327.57$ μs; (b) $t=499$ μs; (c) $t=612.02$ μs; and (d) $t=773.68$ μs.

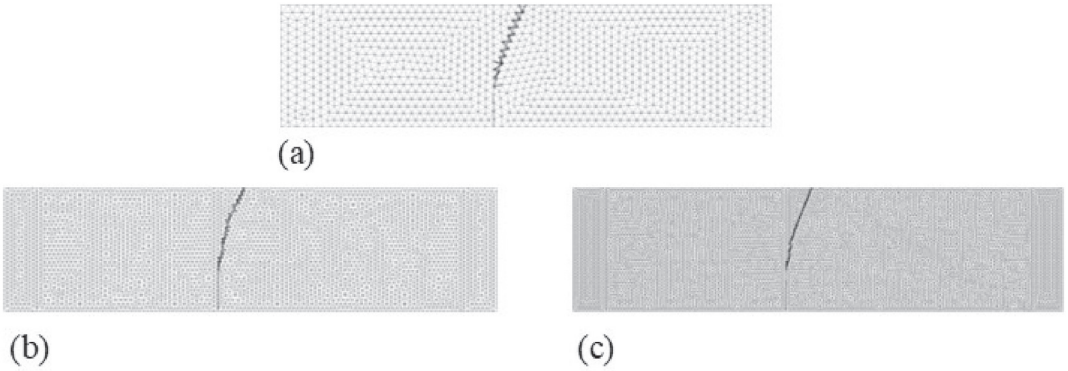

Fig. 25. The crack patterns for different meshes: (a) coarse mesh (b) medium mesh and (c) fine mesh.

experiment in three dimensions. The experimental set-up and the crack path are shown in Fig. 23. A 19 mm offset notch is located at 25.4 mm from beam midspan and then extended by approximately an additional 13 mm depth. Fig. 23(b) shows the averaged crack path obtained in experiments. The crack first grows primarily along an initial angle of $\theta_1 = 10°$ measured from the vertical line, and then it rotates $\theta_2 = 16°$ toward the loading point.

The material properties are: density $\rho = 2400\,\mathrm{kg/m^3}$, Young's modulus $E = 32.3\,\mathrm{GPa}$, and Poisson's ratio $\nu = 0.2$. The impact loading is applied as a prescribed displacement (for more details, refer to [29,30]). The dynamic tensile strength is taken as 7.75 MPa. A linear cohesive crack model is used with the fracture energy of $G_F = 120\,\mathrm{Jm^{-2}}$.

To examine mesh sensitivity, three different triangular meshes were used: (a) a coarse mesh of around 1100 elements; (b) a medium mesh of around 7700 elements; and (c) a fine mesh of around 17200 elements. The crack evolution for only fine mesh is shown in Fig. 24. Similar results are observed for coarse and medium meshes. The final crack paths for these three meshes are illustrated in Fig. 25. The simulation results are listed in Table 2. The results show that the first angle θ_1 has been captured quite accurately with mesh refinement. However, the second angle θ_2 was obtained slightly less than the experimentally obtained value 16°. These results demonstrate that the proposed method can predict the mixed-mode crack propagation paths in three-point bend specimens.

Table 2
Crack propagation angles and timing data resulted from linear complete enriched formulation for the Guo's experiment.

Mesh	Angles(°)		Propagation Time(μs)
	Initial(θ_1)	Final(θ_2)	
Coarse mesh	14.5	9.0	331.6
Medium mesh	11.5	13.2	309.7
Fine mesh	10.8	12.5	295.4

The crack length history and speed for different meshes are shown in Fig. 26. The crack speeds for the linear complete formulation show less mesh dependency than those obtained in [22]. However, the crack speed for the coarse mesh is still higher than the experimental speed. For the medium and fine meshes, the crack speeds compare very well with observed values.

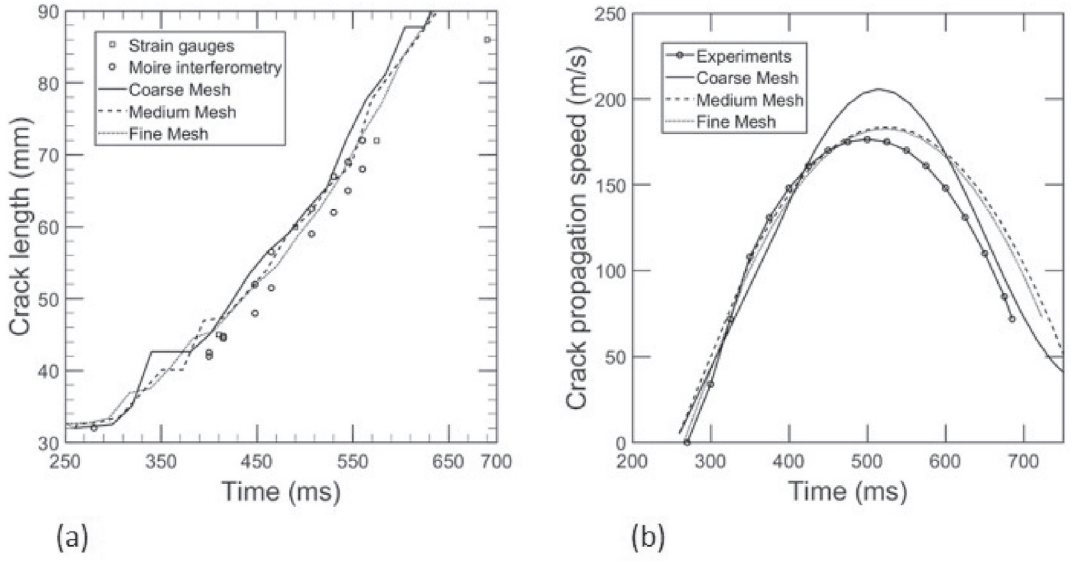

Fig. 26. Crack length history and crack speeds obtained from linear complete enriched formulation for different meshes compared to the Guo's experiment: (a) the crack length histories; and (b) the crack speeds.

5. Conclusion

A linear complete XFEM method with non-nodal enrichment approach was presented. In this method, by appropriately defining two sets of enrichment functions and their associated *physically-based* enrichment variables, the interpolation can reproduce independent linear functions at sides of the interface; linear completeness is a necessary condition for the convergence of finite element based method. Moreover, the enrichments are vanished outside the element domain so that no blending elements appear. The proposed method as a non-nodal XFEM variant facilitates the XFEM implementation in existing finite element programs by dissociating the enrichment definitions from element nodes.

With two static examples from linear elastic fracture mechanics, the convergence of the proposed method was validated. The Dirichlet boundary conditions were simply imposed on the interface, which significantly reduced the error in L^2-norm. To verify the method for modeling dynamic crack propagation, two dynamic examples for which experimental results are available were simulated. In the Kalthoff's experiment, the new method gave negligible mesh dependency on crack speed, in contrast to the conventional XFEM. Moreover, the method resulted very similar crack patterns independent of the mesh. For Guo's experiment, the method successfully reproduced the crack paths and speeds reported from experiments.

An attractive feature of this method is that it can effectively capture the discontinuities in the strains, while leading to a linear complete XFEM. In the future, the proposed technique will be applied to model bi-material problems by imposing appropriate Dirichlet boundary conditions on the *physically-based* enrichment parameters associated to the jumps in derivatives. In addition, a variational formulation based technique to impose discontinuities on the interfaces can be developed based on the idea of Nitsche's method [31–33].

Appendix A. Reproducing independent linear fields on sides of the crack in one dimension

We show that the extended approximation in (4) can reproduce independent linear fields at both sides of the crack. In doing so, we consider

$$\theta(X) = \begin{cases} \alpha_0 + \alpha_1 X & f < 0, \\ \beta_0 + \beta_1 X & f > 0, \end{cases}$$

in which θ is an arbitrary function including both strong and weak discontinuities at $X = X^{\mathrm{c}}$ as shown in Fig. 2(a). The nodal values for such a displacement field are as follows:

$$\begin{cases} \theta_1 = \alpha_0 + \alpha_1 X_1, \\ \theta_2 = \beta_0 + \beta_1 X_2, \\ [\![\theta]\!] = \beta_0 + \beta_1 X^{\mathrm{c}} - \alpha_0 - \alpha_1 X^{\mathrm{c}}, \\ [\![L^e \nabla\theta]\!] = L^e(\beta_1 - \alpha_1). \end{cases} \tag{A.1}$$

In a matrix form, (A.1) can be rewritten as

$$\begin{bmatrix} \theta_1 \\ \theta_2 \\ [\![\theta]\!] \\ [\![L^e \nabla\theta]\!] \end{bmatrix} = \begin{bmatrix} 1 & X_1 & 0 & 0 \\ 0 & 0 & 1 & X_2 \\ -1 & -X^{\mathrm{c}} & 1 & X^{\mathrm{c}} \\ 0 & -L^e & 0 & L^e \end{bmatrix} \begin{bmatrix} \alpha_0 \\ \alpha_1 \\ \beta_0 \\ \beta_1 \end{bmatrix}. \tag{A.2}$$

Applying (5) and (7) to (4) yields the XFEM approximation

$$\begin{bmatrix} \theta^- \\ \theta^+ \end{bmatrix} = \begin{bmatrix} N_1 & N_2 & -N_2 & -s^+ N_2 \\ N_1 & N_2 & N_1 & -s^- N_1 \end{bmatrix} \begin{bmatrix} \theta_1 \\ \theta_2 \\ [\![\theta]\!] \\ [\![L^e \nabla\theta]\!] \end{bmatrix}. \tag{A.3}$$

Substituting nodal values in (A.2) into (A.3) results in

$$\begin{aligned} \begin{bmatrix} \theta^- \\ \theta^+ \end{bmatrix} &= \begin{bmatrix} N_1 & N_2 & -N_2 & -s^+ N_2 \\ N_1 & N_2 & N_1 & -s^- N_1 \end{bmatrix} \begin{bmatrix} 1 & X_1 & 0 & 0 \\ 0 & 0 & 1 & X_2 \\ -1 & -X^{\mathrm{c}} & 1 & X^{\mathrm{c}} \\ 0 & -L^e & 0 & L^e \end{bmatrix} \begin{bmatrix} \alpha_0 \\ \alpha_1 \\ \beta_0 \\ \beta_1 \end{bmatrix} \\ &= \begin{bmatrix} \sum_{I=1}^{2} N_I & \sum_{I=1}^{2} N_I X_I & 0 & 0 \\ 0 & 0 & \sum_{I=1}^{2} N_I & \sum_{I=1}^{2} N_I X_I \end{bmatrix} \begin{bmatrix} \alpha_0 \\ \alpha_1 \\ \beta_0 \\ \beta_1 \end{bmatrix} \\ &= \begin{bmatrix} \alpha_0 + \alpha_1 X \\ \beta_0 + \beta_1 X \end{bmatrix}. \end{aligned}$$

In the above, we used the properties of isoparameteric shape functions given by $\sum_{I=1}^{2} N_I = 1$ and $\sum_{I=1}^{2} N_I X_I = X$.

Appendix B. Reproducing independent linear fields on sides of the crack in two dimensions

Following the same procedure in Appendix A, we consider the following two independent linear fields on sides of the crack as graphically shown in Fig. 5(a).

$$\theta(X,Y)=\begin{cases}\alpha_0+\alpha_1X+\alpha_2Y & f<0,\\ \beta_0+\beta_1X+\beta_2Y & f>0.\end{cases}$$

The nodal values for such a displacement field are given by

$$\begin{cases}\theta_1=\beta_0+\beta_1X_1+\beta_2Y_1,\\ \theta_2=\alpha_0+\alpha_1X_2+\alpha_2Y_2,\\ \theta_3=\alpha_0+\alpha_1X_3+\alpha_2Y_3,\\ [\![\theta]\!]_1=\beta_0+\beta_1X_1^c+\beta_2Y_1^c-\alpha_0-\alpha_1X_1^c-\alpha_2Y_1^c,\\ [\![L_1^c\nabla\theta\cdot\mathbf{e}_1^c]\!]_1=(\beta_1-\alpha_1)(X_3-X_1)+(\beta_2-\alpha_2)(Y_3-Y_1),\\ [\![\theta]\!]_2=\beta_0+\beta_1X_2^c+\beta_2Y_2^c-\alpha_0-\alpha_1X_2^c-\alpha_2Y_2^c,\\ [\![L_2^c\nabla\theta\cdot\mathbf{e}_2^c]\!]_2=(\beta_1-\alpha_1)(X_2-X_1)+(\beta_2-\alpha_2)(Y_2-Y_1).\end{cases}\tag{B.1}$$

where $\mathbf{e}_J^c$'s are calculated as

$$\mathbf{e}_1^c=\frac{1}{L_1^c}\begin{bmatrix}X_3-X_1\\ Y_3-Y_1\end{bmatrix}\quad\text{and}\quad\mathbf{e}_2^c=\frac{1}{L_2^c}\begin{bmatrix}X_2-X_1\\ Y_2-Y_1\end{bmatrix}.$$

In a matrix form, (B.1) can be rewritten as

$$\begin{bmatrix}\theta_1\\ \theta_2\\ \theta_3\\ [\![\theta]\!]_1\\ [\![L_1^c\nabla\theta\cdot\mathbf{e}_1^c]\!]_1\\ [\![\theta]\!]_2\\ [\![L_2^c\nabla\theta\cdot\mathbf{e}_2^c]\!]_2\end{bmatrix}=\begin{bmatrix}0&0&0&1&X_1&Y_1\\ 1&X_2&Y_2&0&0&0\\ 1&X_3&Y_3&0&0&0\\ -1&-X_1^c&-Y_1^c&1&X_1^c&Y_1^c\\ 0&X_1-X_3&Y_1-Y_3&0&X_3-X_1&Y_3-Y_1\\ -1&-X_2^c&-Y_2^c&1&X_2^c&Y_2^c\\ 0&X_1-X_2&Y_1-Y_2&0&X_2-X_1&Y_2-Y_1\end{bmatrix}\begin{bmatrix}\alpha_0\\ \alpha_1\\ \alpha_2\\ \beta_0\\ \beta_1\\ \beta_2\end{bmatrix}.\tag{B.2}$$

Then, the XFEM approximation can be also written in matrix format as follows:

$$\begin{bmatrix}\theta^-\\ \theta^+\end{bmatrix}=\begin{bmatrix}N_1&N_2&N_3&\Psi_1^{u-}&\Psi_1^{\nabla u-}&\Psi_2^{u-}&\Psi_2^{\nabla u-}\\ N_1&N_2&N_3&\Psi_1^{u+}&\Psi_1^{\nabla u+}&\Psi_2^{u+}&\Psi_2^{\nabla u+}\end{bmatrix}\begin{bmatrix}\theta_1\\ \theta_2\\ \theta_3\\ [\![\theta]\!]_1\\ [\![L_1^c\nabla\theta\cdot\mathbf{e}_1^c]\!]_1\\ [\![\theta]\!]_2\\ [\![L_2^c\nabla\theta\cdot\mathbf{e}_2^c]\!]_2\end{bmatrix}.\tag{B.3}$$

Substituting the unknowns in (B.2) into (B.3) gives rise to

$$\begin{bmatrix}\theta^-\\ \theta^+\end{bmatrix}=\begin{bmatrix}N_1&N_2&N_3&\Psi_1^{u-}&\Psi_1^{\nabla u-}&\Psi_2^{u-}&\Psi_2^{\nabla u-}\\ N_1&N_2&N_3&\Psi_1^{u+}&\Psi_1^{\nabla u+}&\Psi_2^{u+}&\Psi_2^{\nabla u+}\end{bmatrix}\times\begin{bmatrix}0&0&0&1&X_1&Y_1\\ 1&X_2&Y_2&0&0&0\\ 1&X_3&Y_3&0&0&0\\ -1&-X_1^c&-Y_1^c&1&X_1^c&Y_1^c\\ 0&X_1-X_3&Y_1-Y_3&0&X_3-X_1&Y_3-Y_1\\ -1&-X_2^c&-Y_2^c&1&X_2^c&Y_2^c\\ 0&X_1-X_2&Y_1-Y_2&0&X_2-X_1&Y_2-Y_1\end{bmatrix}\begin{bmatrix}\alpha_0\\ \alpha_1\\ \alpha_2\\ \beta_0\\ \beta_1\\ \beta_2\end{bmatrix}$$

$$=\sum_{I=1}^{3}\begin{bmatrix}N_I&N_IX_I&N_IY_I&0&0&0\\ 0&0&0&N_I&N_IX_I&N_IY_I\end{bmatrix}\begin{bmatrix}\alpha_0\\ \alpha_1\\ \alpha_2\\ \beta_0\\ \beta_1\\ \beta_2\end{bmatrix}$$

$$= \begin{bmatrix} \alpha_0 + \alpha_1 X + \alpha_2 Y \\ \beta_0 + \beta_1 X + \beta_2 Y \end{bmatrix}.$$

Furthermore, we have extensively used the side-splitter theorem to substitute the parameters $s_K^{\pm}$. Fig B.27 illustrates two different triangles for the computation of s_1^- that leads to two different equations.

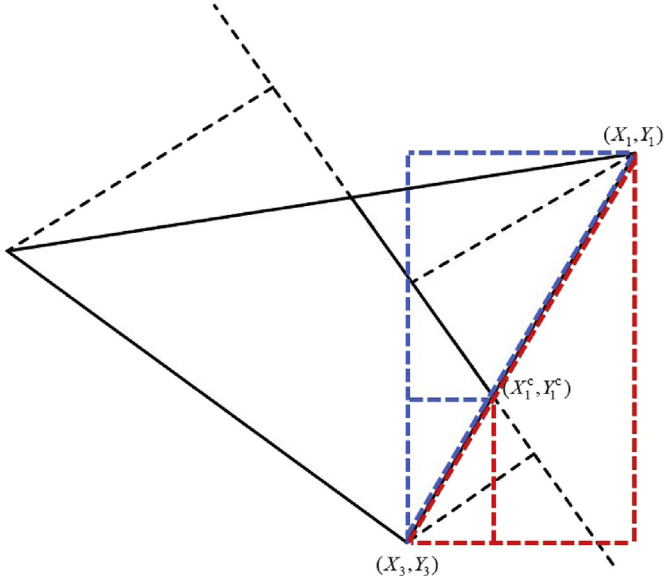

Fig. B.27. Application of side-splitter theorem for the computations of s_1^-; the red triangle gives $s_1^- = (Y_1^c - Y_3)/(Y_1 - Y_3)$ and the blue triangle gives $s_1^- = (X_1^c - X_3)/(X_1 - X_3)$.

Appendix C. Supplementary data

Supplementary data to this article can be found online at https://doi.org/10.1016/j.finel.2018.09.002.

References

[1] N. Moës, J. Dolbow, T. Belytschko, A finite element method for crack growth without remeshing, Int. J. Numer. Meth. Eng. 46 (1) (1999) 131–150.
[2] T. Belytschko, T. Black, Elastic crack growth in finite elements with minimal remeshing, Int. J. Numer. Meth. Eng. 45 (5) (1999) 601–620.
[3] J.M. Melenk, I. Babuška, The partition of unity finite element method: basic theory and applications, Comput. Meth. Appl. Mech. Eng. 139 (1–4) (1996) 289–314.
[4] T.-P. Fries, T. Belytschko, The extended/generalized finite element method: an overview of the method and its applications, Int. J. Numer. Meth. Eng. 84 (3) (2010) 253–304.
[5] T. Belytschko, N. Moës, S. Usui, C. Parimi, Arbitrary discontinuities in finite elements, Int. J. Numer. Meth. Eng. 50 (4) (2001) 993–1013.
[6] J. Chessa, H. Wang, T. Belytschko, On the construction of blending elements for local partition of unity enriched finite elements, Int. J. Numer. Meth. Eng. 57 (7) (2003) 1015–1038.
[7] T.-P. Fries, A corrected xfem approximation without problems in blending elements, Int. J. Numer. Meth. Eng. 75 (5) (2008) 503–532.
[8] T. Belytschko, H. Chen, J. Xu, G. Zi, Dynamic crack propagation based on loss of hyperbolicity and a new discontinuous enrichment, Int. J. Numer. Meth. Eng. 58 (12) (2003) 1873–1905.
[9] G. Zi, H. Chen, J. Xu, T. Belytschko, The extended finite element method for dynamic fractures, Shock Vib. 12 (1) (2005) 9–23.
[10] J.-H. Song, P. Areias, T. Belytschko, A method for dynamic crack and shear band propagation with phantom nodes, Int. J. Numer. Meth. Eng. 67 (6) (2006) 868–893.
[11] T. Chau-Dinh, G. Zi, P.-S. Lee, T. Rabczuk, J.-H. Song, Phantom-node method for shell models with arbitrary cracks, Comput. Struct. 92 (2012) 242–256.
[12] J. Lua, T. Zhang, E. Fang, J.-H. Song, Explicit phantom paired shell element approach for crack branching and impact damage prediction of aluminum structures, Int. J. Impact Eng. 87 (2016) 28–43.
[13] T. Rabczuk, G. Zi, S. Bordas, H. Nguyen-Xuan, A simple and robust three-dimensional cracking-particle method without enrichment, Comput. Meth. Appl. Mech. Eng. 199 (37–40) (2010) 2437–2455.
[14] H. Ren, X. Zhuang, Y. Cai, T. Rabczuk, Dual-horizon peridynamics, Int. J. Numer. Meth. Eng. 108 (12) (2016) 1451–1476.
[15] H. Ren, X. Zhuang, T. Rabczuk, Dual-horizon peridynamics: a stable solution to varying horizons, Comput. Meth. Appl. Mech. Eng. 318 (2017) 762–782.
[16] J. Dolbow, N. Moës, T. Belytschko, Discontinuous enrichment in finite elements with a partition of unity method, Finite Elem. Anal. Des. 36 (3–4) (2000) 235–260.
[17] J. Dolbow, N. Moës, T. Belytschko, An extended finite element method for modeling crack growth with frictional contact, Comput. Meth. Appl. Mech. Eng. 190 (51–52) (2001) 6825–6846.
[18] T.Y. Kim, J. Dolbow, T. Laursen, A mortared finite element method for frictional contact on arbitrary interfaces, Comput. Mech. 39 (3) (2007) 223–235.
[19] T. Menouillard, J. Rethore, A. Combescure, H. Bung, Efficient explicit time stepping for the extended finite element method (x-fem), Int. J. Numer. Meth. Eng. 68 (9) (2006) 911–939.
[20] S. Bordas, P.V. Nguyen, C. Dunant, A. Guidoum, H. Nguyen-Dang, An extended finite element library, Int. J. Numer. Meth. Eng. 71 (6) (2007) 703–732.
[21] I. Nistor, O. Pantalé, S. Caperaa, Numerical implementation of the extended finite element method for dynamic crack analysis, Adv. Eng. Software 39 (7) (2008) 573–587.
[22] I. Asareh, Y.-C. Yoon, J.-H. Song, A numerical method for dynamic fracture using the extended finite element method with non-nodal enrichment parameters, Int. J. Impact Eng. 121 (2018) 63–76.
[23] T. Belytschko, W.K. Liu, B. Moran, K. Elkhodary, Nonlinear Finite Elements for Continua and Structures, John wiley & sons, 2013.
[24] I. Babuška, J.M. Melenk, The partition of unity method, Int. J. Numer. Meth. Eng. 40 (4) (1997) 727–758.
[25] G. Strang, G.J. Fix, An Analysis of the Finite Element Method, vol. 212, Prentice-hall Englewood Cliffs, NJ, 1973.
[26] W.M. Lai, D.H. Rubin, E. Krempl, D. Rubin, Introduction to Continuum Mechanics, Butterworth-Heinemann, 2009.
[27] N. Sukumar, D.L. Chopp, N. Moës, T. Belytschko, Modeling holes and inclusions by level sets in the extended finite-element method, Comput. Meth. Appl. Mech. Eng. 190 (46–47) (2001) 6183–6200.
[28] J. Kalthoff, S. Winkler, Failure mode transition at high rates of shear loading, DGM Informationsgesellschaft mbH, Impact Load. Dynam. Behav. Mater. 1 (1988) 185–195.
[29] Z. Guo, A. Kobayashi, N. Hawkins, Dynamic mixed mode fracture of concrete, Int. J. Solid Struct. 32 (17–18) (1995) 2591–2607.
[30] G. Ruiz, A. Pandolfi, M. Ortiz, Three-dimensional cohesive modeling of dynamic mixed-mode fracture, Int. J. Numer. Meth. Eng. 52 (1–2) (2001) 97–120.
[31] J.A. Nitsche, Über ein Variationsprinzip zur Lösung von Dirichlet-Problemen bei Verwendung von Teilräumen, die keinen Randbedingungen unterworfen sind, Abh. aus dem Math. Semin. Univ. Hambg. 36 (1970/71) 9–15.
[32] T.-Y. Kim, T. Iliescu, E. Fried, B-spline based finite-element method for the stationary quasi-geostrophic equations of the ocean, Comput. Meth. Appl. Mech. Eng. 286 (2015) 168–191.
[33] T.-Y. Kim, J.E. Dolbow, An edge-bubble stabilized finite element method for fourth-order parabolic problems, Finite Elem. Anal. Des. 45 (2009) 485–494.